On Vertex-Centered Unstructured Finite-Volume Methods for Stretched Anisotropic Triangulations

Cécile Viozat, C. Held, K. Mer, Alain Dervieux

INRIA

INSTITUT NATIONAL DE RECHERCHE EN INFORMATIQUE ET EN AUTOMATIQUE

On Vertex-Centered Unstructured Finite-Volume Methods for Stretched Anisotropic Triangulations

C. Viozat, C. Held, K. Mer, A. Dervieux

N° 3464

Juillet 1998

THÈME 4

ISSN 0249-6399

On Vertex-Centered Unstructured Finite-Volume Methods for Stretched Anisotropic Triangulations

C. Viozat*, C. Held†, K. Mer‡, A. Dervieux§

Thème 4 — Simulation et optimisation
de systèmes complexes
Projet SINUS

Rapport de recherche n° 3464 — Juillet 1998 — 50 pages

Abstract: Vertex-Centered Finite-Volume schemes applied to triangulations may present poor accuracy when stretched meshes are used. We introduce a family of variational schemes with three parameters for each triangle and investigate the conditions these parameters must meet in order to have a good behavior on stretched meshes. Some of the resulting schemes are also more qualified for computations on quasi-cartesian meshes than standard schemes with cells limited by medians. We obtain among others the Barth finite volume scheme. These schemes are also related to the so-called MDHR schemes. Application to transonic flows around cylinders and in a booster combustion chamber are discussed.

Key-words: finite-volume method, finite-element method, multidimensional scheme, stretched mesh

* INRIA, BP. 93, 06902 Sophia Antipolis Cedex, France.
† INRIA, BP. 93, 06902 Sophia Antipolis Cedex, France.
‡ Dept. de Mathématiques Appliquées, Université Bordeaux 1, 351 Cours de la Libération, 33405 Talence Cedex, France.
§ INRIA, BP. 93, 06902 Sophia Antipolis Cedex, France.

Unité de recherche INRIA Sophia Antipolis
2004, route des Lucioles, B.P. 93, 06902 Sophia Antipolis Cedex (France)
Téléphone : 04 92 38 77 77 - International : +33 4 92 38 77 77 — Fax : 04 92 38 77 65 - International : +33 4 92 38 77 65

Méthodes de volumes finis non structurés centrées sommets pour les triangulations anisotropiques étirées

Résumé : Les schémas volumes finis centrés sommets appliqués à des triangulations peuvent présenter une mauvaise précision quand des maillages étirés sont utilisés. Nous introduisons une famille de schémas variationnels avec trois paramètres pour chaque triangle et étudions les conditions que ces paramètres doivent vérifier pour avoir un bon comportement en maillage étiré. Certains des schémas obtenus sont aussi plus aptes pour des calculs sur maillages quasi-cartésiens que les schémas standard reposants sur des cellules limitées par des médianes. Nous obtenons entre autres le schéma volumes finis de Barth. Ces schémas sont aussi apparentés aux schémas MDHR. Nous discutons de l'application de ces schémas pour le calcul d'écoulements transsoniques autour d'un cylindre et dans une chambre de combustion de booster.

Mots-clés : Méthode volumes finis, méthode éléments finis, schéma multidimensionnel, maillage étiré

Contents

1 Introduction

Most existing CFD codes rely on finite-volume schemes resulting in a five point stencil for advection. These schemes are of low cost, but of second-order accuracy only on quasi-cartesian meshes. They apply well on regular stretched meshes. However, on highly distorted meshes, accuracy can markedly degrade since the order of accuracy can become much smaller than one. Further, compared to numerical diffusion errors which are made easily smaller by mesh refinement, this kind of error is difficult to detect by the user since, refining the mesh would have a small effect on the refined solution, due to the poor order of this kind of error.

Finite-volume schemes resulting in a seven point stencil can be obtained from vertex formulations on triangles. Some standard choices such as control volumes bounded by segments of medians (so-called *median cells*) are essentially equivalent to the Galerkin variational formulation (centered versions) [18, 8, 2, 15] and enjoy a rather good robustness to distorted meshes as long as they are not stretched. For the Galerkin formulation itself, error estimates show a good behavior for irregular but non-stretched meshes, and for highly stretched meshes which meet a maximum angle condition (e.g. see [14]). Unfortunately, when upwinding that preserves positiveness is introduced, the favorable behavior on unstretched meshes is inherited, but not the robustness to stretching [4, 12]. Indeed, a simple truncation error analysis on cartesian meshes shows that the scheme is not uniformly consistent for arbitrarily stretched meshes [5].

The qualification of the scheme for stretched meshes can be obtained either by relaxing the positivity statement as in the stabilized finite-element method [11] and in artificial viscosity models [13], or by replacing the Galerkin centered approximation with a different one; for example, the shape of the cell can be changed as suggested by Barth [4], or the global approximation can be reconsidered as in the numerous works around multi-dimensional (MD) schemes [16, 19].
For both the Barth approach and the MD approach, the scheme stencil is made in some cases more compact: the containment-circle based dual control volume (that we will call the *Barth cell*) disables fluxes along any edges that are in front of obtuse angles. The MD schemes systematically select only two edge-wise differences per triangle (scalar case). Behind the approximation of the advection terms remains the question of diffusion terms, that are conveniently treated by the Galerkin option only if this treatment is compatible with the advection scheme. Now, it is remarkable that for second order derivatives, the Galerkin triangular approximation (Figure 1) is identical to the usual five point finite difference scheme of the Galerkin quadrangular approximation (Figure 3). For first order derivatives, this is

not true, since non zero coefficients appear in points at the end of diagonals (compare Figure 2 to Figure 4). Considering new advection schemes that reduce on cartesian meshes to a five point approximation seems an interesting standpoint.

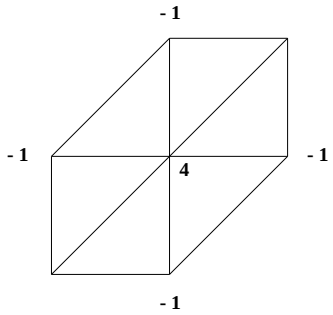

Figure 1: *Illustration of the five point finite-difference stencil for* `triangular` *meshes in the case of the* `diffusion` *equation.*

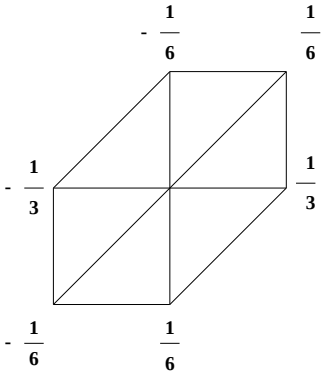

Figure 2: *Illustration of the seven point Galerkin stencil for* `triangular` *meshes in the case of the* `advection` *equation.*

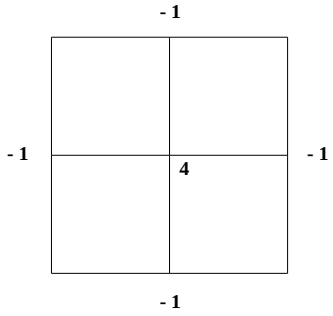

Figure 3: *Illustration of the five point finite-difference stencil for* `quadrilateral` *meshes in the case of the* `diffusion` *equation.*

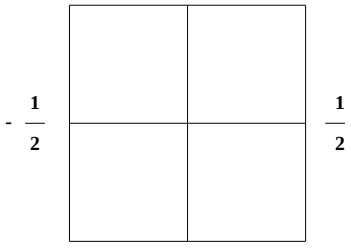

Figure 4: *Illustration of the three point finite-difference stencil for* `quadrilateral` *meshes in the case of the horizontal* `advection` *equation.*

In the present work, we concentrate on amending the vertex centered finite-volume formulation on triangles. A family of cell shapes is defined from a variational argument. Instead of starting from the Galerkin method for obtaining median cells, we introduce a formulation characterized by a modified differentiation operator, in which edgewise gradients are defined on the so-called diamond cell. The use of this diamond derivative reduces the stencil of the scheme, and in the case of cartesian triangulations, the new cell reduces to a rectangular cell. Another feature of the proposed construction is the bridge that is thus established between finite volume, and in particular with special cell shapes as introduced by Barth [4], with finite element (of P1-Galerkin type) and with multidimensional schemes. We develop an analysis of the new family of schemes by proposing a necessary condition for consistency in the presence of stretched meshes. The rest of the scheme construction is more standard: an approximate Riemann solver is introduced for stability purposes, a MUSCL [22] interpolation is applied for increasing the formal order of accuracy, and limiters can be (optionally) added for saving positiveness.

The next three sections of this paper are devoted to the new scheme derivation: variational context (Sec.2), introduction of a diamond derivative (Sec.3) and identification of a family of schemes adapted to stretched meshes (Sec.4). In Section 5, second-order accurate extension is presented. In Section 6, the properties verified by the new scheme are investigated. In Section 7, a set of numerical experiments aiming at showing the accuracy of the selected scheme, and its behavior on stretched and non stretched meshes is presented. In the last part of the paper concluding remarks are given.

2 Variational derivation of the Galerkin Finite-Volume method

The scheme considered in this paper is presented as a modification of the standard P1-Galerkin scheme ; in particular, we adopt the variational formulation. The aim of this section is to recall (with some extra details) the well-known bridge between finite-volume and Galerkin methods [18, 8, 2, 15].

2.1 Variational frame

The two dimensional Euler equations can be written as a system of hyperbolic equations of conservation:

$$W_t + \overrightarrow{\nabla}.\overrightarrow{F}(W) = 0, \quad (1)$$

where $\overrightarrow{F}(W) = (F(W), G(W))^t$.

The variational form is obtained by multiplying Equation (1) by a *test* function ψ_m, and integrating it over an open domain Ω:

$$\int_\Omega \psi_m \, W_t \, d\Omega + \int_\Omega \psi_m \, \overrightarrow{\nabla} \cdot \overrightarrow{F}(W) \, d\Omega \quad = \quad 0, \qquad \forall \; \psi_m \; \in \; L^2(\Omega). \tag{2}$$

Following the standard finite-element method, we approximate W and $\overrightarrow{F}$ by a linear combination of *basis* functions belonging to $H^1(\Omega)$:

$$W \quad = \quad \sum_{n=1}^{N} W_n \varphi_n, \tag{3}$$

and

$$\overrightarrow{F}(W) = \sum_{n=1}^{N} \overrightarrow{F}(W_n) \varphi_n, \tag{4}$$

where N is the number of mesh nodes and φ_n is the finite-element shape function associated with node n. The φ's may not necessarily be chosen identical to the ψ's ("Petrov Galerkin" type formulation).

Substituting Equations (3) and (4) into Equation (2) and replacing $\overrightarrow{\nabla}$ by an approximate gradient $\overrightarrow{\nabla}_h$, we obtain the following set of linear equations:

$$\sum_{n=1}^{N} M_{mn} W_{n,t} + \sum_{n=1}^{N} \overrightarrow{A}_{mn} . \overrightarrow{F}_n \quad = \quad 0, \qquad \forall m = 1, .., N, \tag{5}$$

where

$$M_{mn} \quad = \quad \int_\Omega \varphi_n \psi_m \, d\Omega, \tag{6}$$

$$\overrightarrow{A}_{mn} \quad = \quad \int_\Omega \psi_m \overrightarrow{\nabla}_h \varphi_n \, d\Omega. \tag{7}$$

A classical mass-lumping gives

$$\left(\sum_{n=1}^{N} M_{mn} \right) W_{m,t} + \sum_{n=1}^{N} \overrightarrow{A}_{mn} . \overrightarrow{F}_n \quad = \quad 0, \qquad \forall m = 1, .., N. \tag{8}$$

Definition:
We define properties $(P1)$, $(P2)$ *and* $(P3)$ *by:*

$$\begin{aligned} &(P1) \quad \overrightarrow{A}_{mm} = 0, && \forall m = 1,..,N, \\ &(P2) \quad \sum_{n=1}^{N} \overrightarrow{A}_{mn} = 0, && \forall m = 1,..,N, \\ &(P3) \quad \overrightarrow{A}_{mn} = -\overrightarrow{A}_{nm}, && \forall m,n = 1,..,N. \end{aligned} \tag{9}$$

■

Proposition 1 [8, 15, 18]:
If Properties $(P1)$, $(P2)$ *and* $(P3)$ *hold, the approximation described in (8) is equivalent to the following finite-volume type method*

$$Area(C_m)\, W_{m,t} + \sum_{\substack{n=1 \\ n \neq m}}^{N} \overrightarrow{\eta}_{mn} \cdot \frac{\overrightarrow{F}_m + \overrightarrow{F}_n}{2} = 0, \ \forall m = 1,..,N, \tag{10}$$

where $Area(C_m) = \sum_{n=1}^{N} M_{mn}$ *is the area of a (at least virtual) finite-volume control volume* C_m *and* $\overrightarrow{\eta}_{mn} = 2\,\overrightarrow{A}_{mn}$ *is the mean normal vector occuring in the finite-volume flux integration between nodes* m *and* n. ■

2.2 Lagrange-Galerkin particular case

For the Lagrange-Galerkin formulation ($\varphi_m = \psi_m$ with Lagrange interpolation and $\overrightarrow{\overline{\nabla}_h} = \overrightarrow{\overline{\nabla}}$), Properties (P1), (P2) and (P3) are satisfied [8].

In particular, if $\varphi_m (= \psi_m)$ are P1-Lagrange basis functions (i.e. continuous, piecewise linear on each triangle and equal to 1 at node m and 0 at the other nodes), then it is well-known that Equation (8) is equivalent to Equation (10) in which the cell C_m (see Figure 5) is delimited by the medians of the neighboring triangles of the vertex m and $\overrightarrow{\eta}_{mn}$ is the mean outward normal vector to the interface $C_m \cap C_n$.

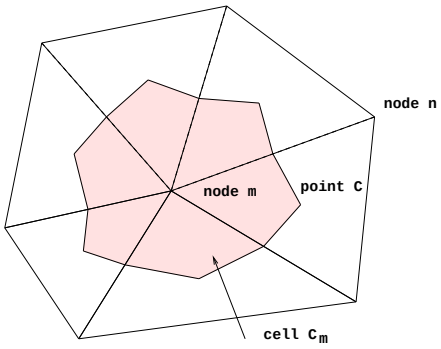

Figure 5: *Cell built around node* m.

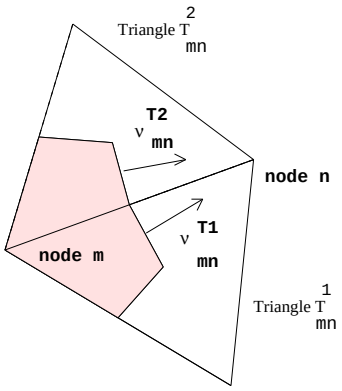

Figure 6: *The mean normal vector occuring in the finite volume flux integration between nodes m and n is* $\vec{\eta}_{mn} = \vec{\nu}^{T1}_{mn} + \vec{\nu}^{T2}_{mn}$.

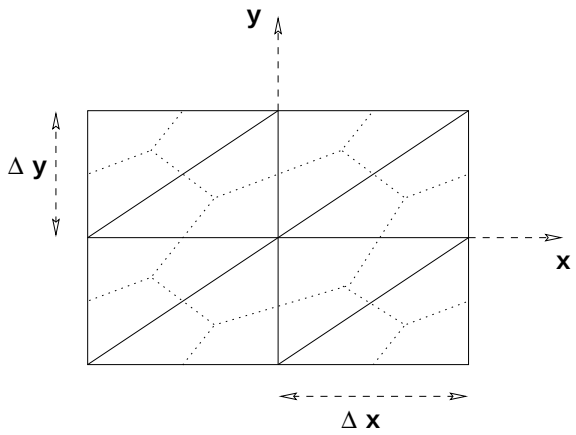

Figure 7: *Cartesian mesh, and median cells in dotted lines.*

Then, the so-called median finite-volume method (as in Baba-Tabata [3]) is a natural variation of the finite-element method. An upwind version is easily built by introducing some flux splitting. In the case of the scalar advection equation

$$w_t + div(\overrightarrow{V}\ w) = 0, \tag{11}$$

where $\overrightarrow{V} = (a, b)^t$ is a constant vector and using the usual "Donor Cell" splitting, Equation (10) becomes:

$$Area(C_m)\, w_{m,t} + \sum_{\substack{n=1 \\ n \neq m}}^{N} \left[\frac{\overrightarrow{V}.\overrightarrow{\eta}_{mn}}{2} (w_m + w_n) + \mid \frac{\overrightarrow{V}.\overrightarrow{\eta}_{mn}}{2} \mid (w_m - w_n) \right] = 0, \forall m = 1, .., N. \tag{12}$$

A truncation error analysis of Scheme (12) applied to the case of a family of skewed meshes as described in Figure 7, with $\Delta x \neq \Delta y$, yields:

$$\begin{aligned}
w_t = \quad & -a && w_x \\
& -b && w_y \\
& + \frac{1}{6} \left[\mid b\frac{(\Delta x)^2}{\Delta y} - 2\, a\, \Delta x \mid + \mid b\frac{(\Delta x)^2}{\Delta y} + a\, \Delta x \mid \right] && w_{xx} \\
& + \frac{1}{3} \mid b\Delta x + a\Delta y \mid && w_{xy} \\
& + \frac{1}{6} \left[\mid 2\, b\, \Delta y - a\, \frac{(\Delta y)^2}{\Delta x} \mid + \mid b\, \Delta y + a\, \frac{(\Delta y)^2}{\Delta x} \mid \right] && w_{yy} \\
& - \frac{1}{6}\, a\, (\Delta x)^2 && w_{xxx} \\
& - \frac{1}{6} (b\, \Delta x + a\Delta y)\Delta x && w_{xxy} \\
& - \frac{1}{6} (b\, \Delta x + a\Delta y)\Delta y && w_{xyy} \\
& - \frac{1}{6}\, b\, (\Delta y)^2 && w_{yyy} \\
& + O\left(\Delta x^3, \Delta y^3, \frac{\Delta x^4}{\Delta y}, \frac{\Delta y^4}{\Delta x} \right),
\end{aligned} \tag{13}$$

in which the function $O\left(\Delta x^3, \Delta y^3, \frac{\Delta x^4}{\Delta y}, \frac{\Delta y^4}{\Delta x}\right)$ holds for a term that is asymptotically smaller than Δx^3, Δy^3, $\frac{\Delta x^4}{\Delta y}$ or $\frac{\Delta y^4}{\Delta x}$.

It is clear that Scheme (12) is consistent if $\frac{\Delta x}{\Delta y}$ and $\frac{\Delta y}{\Delta x}$ are uniformly bounded. Conversely, this scheme may lose its consistency in the case of stretched meshes. Indeed, for an increasing stretching, we may have $\frac{\Delta x^2}{\Delta y} \to \infty$ if the stretching direction is along the x axis, or $\frac{\Delta y^2}{\Delta x} \to \infty$ if it is along the y axis, thus the first-order terms of the truncation error will increase.

The lack of accuracy for stretched meshes is the main drawback of this standard finite-volume method. Several ways to go around this drawback have been proposed [6, 4, 12]. They involve changing the shape of the finite-volume cells. Analysing the resulting schemes with respect to the standard Galerkin variational formulation is rather difficult; therefore, we propose a new variational frame for the definition of new finite-volume schemes.

3 Diamond variant

3.1 Definition of the main choices

In order to develop a method accurate on stretched meshes, and getting inspiration from the multidimensional schemes building (e.g. see [20]), we consider Equation (8) with the following choices:

- **A point** C is chosen on each triangle (C is not necessarily located at centroid).

- **Test functions:**

$$\psi_m^C = \chi_{C_m}, \tag{14}$$

where χ_{C_m} denotes the characteristic function (i.e. the function is equal to 1 on the area C_m and 0 elsewhere) and C_m is the cell built around node m by joining for each triangle around m the middle of edges to a point C in the triangle (see Figure 5).

- **Basis functions:** φ_n are P1-Lagrange basis functions.

• **Discretized gradient operator:**

We consider a triangle T (assumed not degenerated) of vertices i, j and k, and a given point C of T. The triangle T is numbered anti-clockwise.

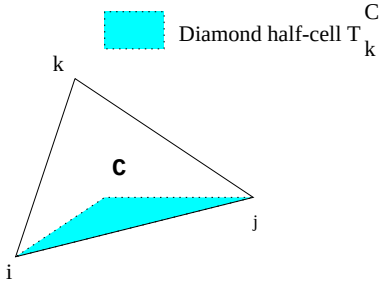

Figure 8: *Illustration of the diamond half-cell T_k^C.*

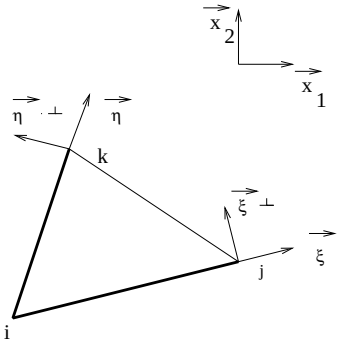

Figure 9: *The global referencial $(\vec{x_1}, \vec{x_2})$ and the local referencial $(\vec{\xi}, \vec{\eta})$.*

Definition:

The diamond half-cell related to the edge ij is the triangle T_k^C of vertices i, j and C (see Figure 8). Similarly, the diamond half-cell related to the edges jk and ki are respectively the triangles T_i^C of vertices j, k and C, and T_j^C of vertices k, i and C. ■

We denote by $\lambda_i(x,y)$, $\lambda_j(x,y)$ and $\lambda_k(x,y)$ the barycenter coordinates of T. For any point $C(x_C, y_C)$ we consider

$$\begin{aligned} \lambda_i^C &= \lambda_i(x_C, y_C) = \frac{Area(T_i^C)}{Area(T)}, \\ \lambda_j^C &= \lambda_j(x_C, y_C) = \frac{Area(T_j^C)}{Area(T)}, \\ \lambda_k^C &= \lambda_k(x_C, y_C) = \frac{Area(T_k^C)}{Area(T)}. \end{aligned} \tag{15}$$

The local coordinate system $(\vec{\xi},\ \vec{\eta})$ is defined by (see Figure 9)

$$\vec{\xi} = \frac{\vec{ij}}{\parallel \vec{ij} \parallel}, \quad \vec{\eta} = \frac{\vec{ik}}{\parallel \vec{ik} \parallel}.$$

Definition of the diamond derivation in the local coordinate system $(\vec{\xi},\ \vec{\eta})$:

Let f be a function defined on triangle T; the diamond derivation of f in the local coordinate system $(\vec{\xi},\vec{\eta})$ is given by

$$\frac{\partial_h f}{\partial_h \xi}|_T = \frac{\chi_{T_k^C}}{\lambda_k^C}\ \frac{f(j)-f(i)}{\parallel \vec{ji} \parallel}, \tag{16}$$

$$\frac{\partial_h f}{\partial_h \eta}|_T = \frac{\chi_{T_j^C}}{\lambda_j^C}\ \frac{f(k)-f(i)}{\parallel \vec{ki} \parallel}, \tag{17}$$

where χ denotes the characteristic function.

In the case where $f(\xi,\eta)|_T$ is a linear function, the following properties hold:

$$\begin{aligned} \int_T \frac{\partial_h f}{\partial_h \xi} d\xi\ d\eta &= \int_T \frac{\partial f}{\partial \xi} d\xi\ d\eta, \\ \int_T \frac{\partial_h f}{\partial_h \eta} d\xi\ d\eta &= \int_T \frac{\partial f}{\partial \eta} d\xi\ d\eta, \end{aligned} \tag{18}$$

since

$$\int_T \frac{\chi_{T_k^C}}{\lambda_k^C} dT = Area(T). \tag{19}$$

Definition of the diamond derivation in the global coordinate system $(\vec{x_1},\vec{x_2})$:

Once derivatives have been computed in directions ξ and η, we can deduce derivatives in all directions.

The relation between the global referential $(\vec{x_1},\vec{x_2})$ and the local referential $(\vec{\xi},\vec{\eta})$ is given by:

$$\overrightarrow{x_l} = \alpha_l\ \overrightarrow{\xi} + \beta_l\ \overrightarrow{\eta}, \qquad l = 1,\ 2, \tag{20}$$

where

$$\alpha_l = \frac{\overrightarrow{x_l}\,.\,\overrightarrow{\eta}^{\perp}}{\overrightarrow{\xi}\,.\,\overrightarrow{\eta}^{\perp}}, \qquad \beta_l = \frac{\overrightarrow{x_l}\,.\,\overrightarrow{\xi}^{\perp}}{\overrightarrow{\eta}\,.\,\overrightarrow{\xi}^{\perp}}, \qquad l = 1,\ 2. \tag{21}$$

In Equation (21), as well as in the rest of the paper, we denote by $\vec{v}^{\perp}$ the vector of components $(-v_y, v_x)$ (where (v_x, v_y) are the components of $\vec{v}$).

We can rewrite the coefficients given in Equation (21) in terms of the coordinates of triangle T:

$$\begin{pmatrix} \alpha_1 \\ \alpha_2 \end{pmatrix} = \frac{\vec{ki}^{\perp} \parallel \vec{ij} \parallel}{2\, Area(T)}, \qquad \begin{pmatrix} \beta_1 \\ \beta_2 \end{pmatrix} = \frac{\vec{ij}^{\perp} \parallel \vec{ik} \parallel}{2\, Area(T)}. \tag{22}$$

The derivative of a function $f(x_1, x_2)$ in the global referential can be written with regard to the local referential in the following manner :

$$\frac{\partial_h f}{\partial_h x_l}|_T \;=\; \alpha_l \frac{\partial_h f}{\partial_h \xi}|_T \;+\beta_l \frac{\partial_h f}{\partial_h \eta}|_T, \qquad l = 1,\, 2. \tag{23}$$

Substituting Equations (16) and (17) into Equation (23) we finally obtain the diamond derivation in the global coordinate system:

$$\frac{\partial_h f}{\partial_h x_l}|_T \;=\; \alpha_l \frac{\chi_{T_k^C}}{\lambda_k^C} \frac{f(j) - f(i)}{\parallel \vec{ji} \parallel} + \;\; \beta_l \frac{\chi_{T_j^C}}{\lambda_j^C} \frac{f(k) - f(i)}{\parallel \vec{ki} \parallel}, \qquad l = 1,\, 2, \tag{24}$$

which can also be written using Equation (22) as

$$\nabla_h f|_T \;=\; \frac{\vec{ki}^{\perp}}{2} \frac{\chi_{T_k^C}}{Area(T)\, \lambda_k^C} \left(f(j) - f(i)\right) \;+\; \frac{\vec{ij}^{\perp}}{2} \frac{\chi_{T_j^C}}{Area(T)\, \lambda_j^C} \left(f(k) - f(i)\right). \tag{25}$$

If $(\vec{ij}, \vec{ik})$ defines a cartesian coordinate system, this derivative is identical to the usual derivative. In general it is a different one. We summarize the definition of the diamond scheme as follows:

Definition
We call diamond scheme with ij and ik as the two sides chosen for directional splitting the following variational form of Equation (1)

$$\int_\Omega \psi_m^C\, W_t \, d\Omega + \int_\Omega \psi_m^C\, \overrightarrow{\nabla}_h \cdot \overrightarrow{F}(W)\, d\Omega \;=\; 0, \tag{26}$$

$$\overrightarrow{F}(W) = \sum_{n=1}^{N} \overrightarrow{F}(W_n)\varphi_n, \tag{27}$$

where φ_n are P1-Lagrange basis functions, $\psi_m^C = \chi_{C_m}$ are the test functions and the diamond derivation is given by (25).■

3.2 Passing to centered finite volumes

We now apply Proposition 1 to the new context. Let us check that properties $(P1)$, $(P2)$ and $(P3)$ hold for the diamond method (26)-(27)-(25):

- **Verification of** $(P1)$

  To show that $(P1)$ holds, we need to compute $\overrightarrow{A}_{mm}$.

  By definition (7), we have

$$(A_{mm})_l = \sum_{T \in N(m)} \int_T \psi_m^C \frac{\partial_h \varphi_m}{\partial_h x_l} d\Omega, \qquad l = 1, 2, \tag{28}$$

  where $N(m)$ denotes the neighboring triangles of the vertex m.

  Using the definition of the diamond derivation (25), we obtain:

$$(A_{mm})_l = \sum_{T \in N(m)} \frac{Area(T)}{2} \frac{\partial \varphi_m}{\partial x_l}|_T, \qquad l = 1, 2. \tag{29}$$

  Moreover, since φ_m is a P1-Lagrange basis function we can write

$$\int_T \varphi_m \, d\Omega = \frac{Area(T)}{3}.$$

  Therefore (29) can be written as

$$(A_{mm})_l = \frac{3}{2} \sum_{T \in N(m)} \int_T \varphi_m \frac{\partial \varphi_m}{\partial x_l} d\Omega, \qquad l = 1, 2. \tag{30}$$

  Since $\varphi_m \dfrac{\partial \varphi_m}{\partial x_l} = \dfrac{1}{2} \dfrac{\partial (\varphi_m)^2}{\partial x_l}$, after an integration by parts we obtain

$$\begin{aligned} \overrightarrow{A}_{mm} &= \frac{3}{4} \sum_{T \in N(m)} \int_{\partial T} (\varphi_m)^2 \vec{n} d\sigma, \\ &= \frac{3}{4} \int_{\partial \Omega} (\varphi_m)^2 \vec{n} d\sigma, \end{aligned} \tag{31}$$

where $\partial\Omega$ denotes the boundary of the support of the φ_m function and $\vec{n}$ is the exterior unitary normal.

Since $\varphi_m = 0$ on $\partial\Omega$, we have $\overrightarrow{A}_{mm} = 0$. ■

- **Verification of** $(P2)$

  To show that $(P2)$ holds, we need to compute $\sum_n \overrightarrow{A}_{mn}$.

  By definition (see Equation (7)), we have:

$$\sum_n (A_{mn})_l = \sum_n \int_\Omega \psi_m^C \frac{\partial_h \varphi_n}{\partial_h x_l} d\Omega \qquad l = 1, 2. \tag{32}$$

  Equation (32) can be written as

$$\sum_n (A_{mn})_l = \int_\Omega \psi_m^C \frac{\partial_h \varphi_{sum}}{\partial_h x_l} d\Omega, \qquad l = 1, 2 \tag{33}$$

  where

$$\varphi_{sum} = \sum_{n=1}^{N} \varphi_n \, .$$

  Moreover, for linear functions, using properties (18), we can write

$$\sum_n (A_{mn})_l = \int_\Omega \psi_m^C \frac{\partial \varphi_{sum}}{\partial x_l} d\Omega, \qquad l = 1, 2. \tag{34}$$

  Since the function φ_n is a P1-Lagrange function, we have:

$$\varphi_{sum} = 1. \tag{35}$$

  Sustituting Equation (35) into Equation (34), we obtain $\sum_n \overrightarrow{A}_{mn} = 0$.■

- **Verification of** $(P3)$

  To show that $(P3)$ holds, we need to compute $\overrightarrow{A}_{mn}$ and $\overrightarrow{A}_{nm}$.

In the case where $m \neq n$, according to Equation (7), we can write

$$(A_{mn})_l = \sum_{T=T^1_{mn},T^2_{mn}} \left(A^T_{mn}\right)_l , \qquad l = 1, 2, \tag{36}$$

where

$$\left(A^T_{mn}\right)_l = \int_T \psi^C_m \frac{\partial_h \varphi_n}{\partial_h x_l} dT, \qquad l = 1, 2. \tag{37}$$

In Equation (36), T^1_{mn} and T^2_{mn} denote the two triangles having mn as a common edge (see Figure 6).

Substituting Equation (25) into Equation (37) we obtain:

$$\begin{aligned} \overrightarrow{A^T}_{nm} &= \frac{\vec{ki}^{\perp}}{2} \left(\varphi_n(j) - \varphi_n(i)\right) \int_T \psi^C_m \left[\frac{\chi_{T^C_k}}{Area(T)\, \lambda^C_k}\right] dT \\ &+ \frac{\vec{ij}^{\perp}}{2} \left(\varphi_n(k) - \varphi_n(i)\right) \int_T \psi^C_m \left[\frac{\chi_{T^C_j}}{Area(T)\, \lambda^C_j}\right] dT. \end{aligned} \tag{38}$$

Taking into account the definition of λ^C_k (15) and the definition of ψ^C_m (14) we can write Equation (38) as:

$$\begin{aligned} \overrightarrow{A^T}_{nm} &= \frac{\vec{ki}^{\perp}}{2} \left(\varphi_n(j) - \varphi_n(i)\right) \int_{T \cap C_m} \frac{\chi_{T_k}}{Area(T_k)} dx_1 dx_2 \\ &+ \frac{\vec{ij}^{\perp}}{2} \left(\varphi_n(k) - \varphi_n(i)\right) \int_{T \cap C_m} \frac{\chi_{T_j}}{Area(T_j)} dx_1 dx_2. \end{aligned} \tag{39}$$

The numerical computation of the terms involved in Equation (39) is straightforward:

$$\begin{aligned}
\int_{T\cap C_m} \frac{\chi_{T_k}}{Area(T_k)} dx_1 dx_2 &= \begin{cases} 1/2 & \text{if} \quad m=i, \\ 1/2 & \text{if} \quad m=j, \\ 0 & \text{if} \quad m=k, \end{cases} \\
\int_{T\cap C_m} \frac{\chi_{T_j}}{Area(T_j)} dx_1 dx_2 &= \begin{cases} 1/2 & \text{if} \quad m=i, \\ 0 & \text{if} \quad m=j, \\ 1/2 & \text{if} \quad m=k, \end{cases} \\
\varphi_n(j) - \varphi_n(i) &= \begin{cases} -1 & \text{if} \quad n=i, \\ 1 & \text{if} \quad n=j, \\ 0 & \text{if} \quad n=k, \end{cases} \\
\varphi_n(k) - \varphi_n(i) &= \begin{cases} -1 & \text{if} \quad n=i, \\ 0 & \text{if} \quad n=j, \\ 1 & \text{if} \quad n=k. \end{cases}
\end{aligned} \tag{40}$$

Substituting Equations (40) into Equation (39), we obtain

$$\overrightarrow{A^T}_{nm} = \begin{cases} \vec{ki}^{\perp}/4 & \text{if} \quad \vec{mn} = \vec{ij}, \\ \vec{ik}^{\perp}/4 & \text{if} \quad \vec{mn} = \vec{ji}, \\ \vec{ij}^{\perp}/4 & \text{if} \quad \vec{mn} = \vec{ik}, \\ \vec{ji}^{\perp}/4 & \text{if} \quad \vec{mn} = \vec{ki}, \\ 0 & \text{if} \quad \vec{mn} = \vec{jk}, \\ 0 & \text{if} \quad \vec{mn} = \vec{kj}. \end{cases} \tag{41}$$

From Equation (41), we can verify that $\overrightarrow{A^T}_{mn} = -\overrightarrow{A^T}_{nm}$, therefore $\overrightarrow{A}_{mn} = -\overrightarrow{A}_{nm}$.■

According to Proposition 1, we have the lemma:

Lemma 3.1 *The diamond method with ij and ik as the two sides chosen for directional splitting (26)-(27)-(25) is equivalent to the finite-volume type method (10) with*

$$(\eta_{mn})_l = \sum_{T=T^1_{mn},T^2_{mn}} \left(\nu^T_{mn}\right)_l, \qquad l=1,2, \tag{42}$$

where

$$\left(\nu^T{}_{mn}\right)_l = \begin{cases} (\vec{ki})^\perp/2, & \textit{if} \quad \vec{mn} = \vec{ij}, \\ (\vec{ij})^\perp/2, & \textit{if} \quad \vec{mn} = \vec{ik}, \\ 0, & \textit{if} \quad \vec{mn} = \vec{jk}. \end{cases} \tag{43}$$

$Area(C_m)$ is the area of the cell chosen for building the test functions.

Remark

The normal vectors $\vec{\eta}_{mn}$ obtained are the normal vectors to a cell defined on each triangle by joining the middle point of the two chosen sides for the diamond derivation to the middle point of the third side (see Figure (11.a)). ■

3.3 Qualification of a diamond scheme for cartesian meshes

A truncation error analysis of Scheme (12) using the diamond method based on the *two smallest sides*, applied to the case of a family of skewed meshes as described in Figure 7, with $\Delta x \neq \Delta y$, yields:

$$\begin{aligned} w_t = \quad & -a && w_x \\ & -b && w_y \\ & +\frac{1}{2} \mid a \mid \Delta x && w_{xx} \\ & +\frac{1}{2} \mid b \mid \Delta y && w_{yy} \\ & -\frac{1}{2}\, a\,(\Delta x)^2 && w_{xxx} \\ & -\frac{1}{2}\, b\,(\Delta y)^2 && w_{yyy} \\ & + O\left(\Delta x^3, \Delta y^3\right), \end{aligned} \tag{44}$$

in which the function $O\left(\Delta x^3, \Delta y^3\right)$ holds for a term that is asymptotically smaller than Δx^3 or Δy^3.

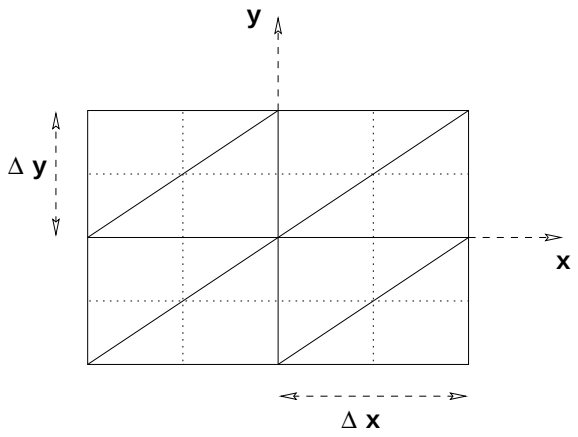

Figure 10: *Cartesian mesh, and cells (in dotted lines) obtained with the diamond scheme using the two smallest sides.*

Conversely to the truncation error obtained for the median finite-volume method the diamond method based on the two smallest sides leads to a truncation error which contains no terms in $\frac{\Delta x}{\Delta y}$ or $\frac{\Delta y}{\Delta x}$. Consistency to stretching is obtained. As shown in Figure 10, in this case, cells reduce to quadrilateral cells. The scheme results in a five point stencil.

3.4 Bridge with centered MDHR

In this section, we analyse the relationship between the dual diamond method and the multidimensional scheme of Sidilkover [20]. We show that, in the case of a 2D scalar advection equation, the dual diamond method in which the point C is chosen as the gravity center of the triangle, is similar to the centered multidimensional scheme of Sidilkover.

The discretization (26)-(27)-(25) (or equivalently (42)-(43)) writes, for a given vertex l:

$$\begin{aligned} & Area(C_I)\frac{dw_l}{dt} \\ + & \sum_{T\ni l} Area(T)\,\gamma\,\frac{w(j)-w(i)}{\parallel \vec{ij} \parallel}\int_{T\cap C_I}\frac{\chi_{T_k}}{Area(T_k)}dx_1dx_2 \\ + & \sum_{T\ni l} Area(T)\,\delta\,\frac{w(k)-w(i)}{\parallel \vec{ik} \parallel}\int_{T\cap C_I}\frac{\chi_{T_j}}{Area(T_j)}dx_1dx_2 \\ = & \ 0, \end{aligned} \tag{45}$$

where the sums are taken for any triangle T of vertices i, j and k which has l as vertex (l is either i or j or k), and

$$\gamma = a\alpha_1 + b\alpha_2, \qquad \delta = a\beta_1 + b\beta_2, \tag{46}$$

with coefficients $\alpha_1, \alpha_2, \beta_1$ and β_2 given in (22).

Computing this expression in the three cases $l = i, j, k$ we obtain the following discrete scheme:

$$\left\{\begin{array}{lcl} Area(C_i)\frac{dw_i}{dt} & := & \frac{1}{2}(R^\xi + R^\eta), \\ Area(C_j)\frac{dw_j}{dt} & := & \frac{1}{2}R^\xi, \\ Area(C_k)\frac{dw_k}{dt} & := & \frac{1}{2}R^\eta. \end{array}\right. \tag{47}$$

where we define the following quantities, which are some finite-difference approximations of the derivatives of w on triangle T (see Figure 9):

$$\left\{\begin{array}{lcl} R^\xi & = & -Area(T)\,\gamma\,\frac{w_j - w_i}{\parallel \vec{ij} \parallel}, \\ R^\eta & = & -Area(T)\,\delta\,\frac{w_k - w_i}{\parallel \vec{ik} \parallel}. \end{array}\right. \tag{48}$$

The system of Equations (47) is identical to the *fluctuation distribution formulae* of Sidilkover (as presented Equation (7) in [20]) for the case of a 2D scalar advection equation,

i.e. we have the *centered* version of the multidimensional scheme of Sidilkover.
This illustrates in particular that this *centered* MDHR version is a finite volume scheme (i.e. a Lax-Wendroff theorem for convergence towards weak solution can be directly applied). For convergence towards weak solutions in the case of the *upwind* MDHR version (i.e. the narrow scheme), we refer to [1].

3.5 Bridge towards distributive schemes

Distributive schemes [21, 7] rely on a basic vertex-distribution of the element-by-element flux integral; for the state of simplicity, the time derivative is put under finite volume form:

$$Area(C_i)\frac{\partial w_i}{\partial t} \;=\; \sum_T \beta_i^T \Phi^T,$$

where

$$\Phi^T \;=\; \int_T \nabla\cdot\vec{F^h} dx_1 dx_2 \;=\; \int_{\partial T} (\vec{V}\cdot\vec{n}) w \; d\sigma \;,$$

where $\vec{F^h}$ is an approximation of $\vec{F} = \vec{V} w$.

Let us define the following functions that are constant on each triangle:

$$\begin{aligned}
\beta_i^T &= \frac{1}{2\Phi_T}\,(R_\xi + R_\eta),\\
\beta_j^T &= \frac{1}{2\Phi_T}\,R_\xi,\\
\beta_k^T &= \frac{1}{2\Phi_T}\,R_\eta,
\end{aligned}$$

where $\Phi^T \neq 0$. We deduce that the above family of centered schemes ((42)-(43) or (47)) belongs to the family of *distributive schemes*. We observe that this implies that we can also write them under a purely *Petrov-Galerkin* formulation, i.e. with the usual *Galerkin basis functions* φ_i and with an exact derivation of them (in contrast to the diamond derivation of the first sections). It is indeed enough to introduce in the variational formulation the following *test* functions:

$$Area(C_i)\frac{\partial w_i}{\partial t} \;=\; \int_\Omega \nabla\cdot\vec{F^h}\;\psi_i^{PG} d\Omega$$

$$\psi_i^{PG}|_T \;=\; \varphi_i|_T \;+\; \beta_i^T \;-\; 1/3\,.$$

Since the β_i^T are constant by element, the gradient of the test functions is identical to that of the Galerkin basis function *in* each triangle, but not through the boundary of the triangles. However, it is usual to consider that this allows us to replace in *diffusive terms* the Petrov-Galerkin ψ_i by the Galerkin φ_i:

$$Area(C_i)\frac{\partial w_i}{\partial t} \;=\; \int_\Omega \nabla\cdot\vec{F^h}\;\psi_i^{PG}d\Omega \;+\; \int_{\partial\Omega}\nabla w\cdot\nabla\varphi_i\;d\sigma$$

Such strategies are adopted in the Petrov-Galerkin works [11] and in distributive schemes works [17].

4 Analysis of high stretching

The three possible options (see Figure 11) that we have defined for any triangle will allow the definition of a family of schemes which will rely on a barycenter between the three possible diamond derivatives with weighting coefficients defined on each triangle. Not all the schemes of this family are consistent for arbitrary stretched meshes. The purpose of this section is to build necessary conditions for a scheme of the above family to be consistent with arbitrary meshes.

4.1 Barycentered Formulation

Let us denote by α_i, α_j and α_k the barycenter coefficients of schemes DI, DJ and DK, for each triangle. The diamond method with ij and ik as the two sides chosen for directional splitting corresponds to the case where (α_i, α_j, α_k) = (1, 0, 0). We now consider the family of schemes combining the three possible diamond schemes (see Figure 11), by replacing Equation (43) by ($\alpha_i+\alpha_j+\alpha_k=1$)

$$\vec{\nu}_{mn}^T \;=\; \begin{cases} \left(\alpha_i\,(\vec{ki})^\perp+\alpha_j\,(\vec{kj})^\perp\right)/2 & \text{if}\quad \vec{mn}=\vec{ij},\\ \left(\alpha_i\,(\vec{ij})^\perp+\alpha_k\,(\vec{kj})^\perp\right)/2 & \text{if}\quad \vec{mn}=\vec{ik},\\ \left(\alpha_j\,(\vec{ij})^\perp+\alpha_k\,(\vec{ik})^\perp\right)/2 & \text{if}\quad \vec{mn}=\vec{jk}, \end{cases} \tag{49}$$

We will now analyze the truncation error in three different contexts of uniform meshes. This analysis will give us necessary conditions on the coefficients of the barycenter (α_i, α_j, α_k), to obtain consistent schemes.

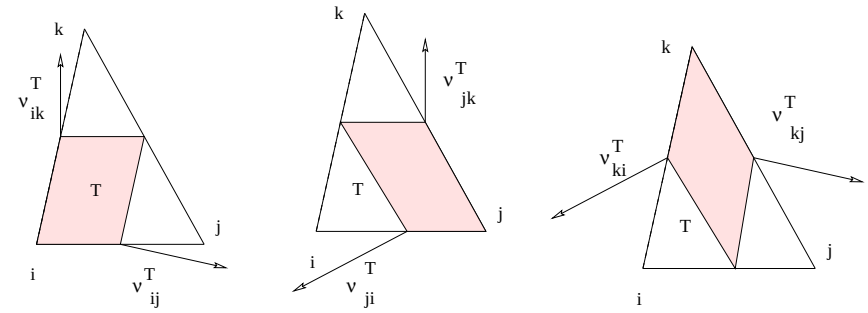

(α_i, α_j, α_k) = (1, 0, 0) (α_i, α_j, α_k) = (0, 1, 0) (α_i, α_j, α_k) = (0, 0, 1)

(a) (b) (c)

Figure 11: *The three possible diamond schemes: (a) the scheme DI, (b) the scheme DJ and (c) the scheme DK.*

4.2 A uniform triangulation model

We will not derive an error analysis applicable to any *unstructured* stretched meshes. Instead of this, we will concentrate on a typical example of a sequence of *structured* meshes with an increasing fineness, and, at the same time, an increasing stretching.

Returning to the advection example (11) of Section 2.2, we can extract the truncation error from the new family of schemes on the triangulation $\mathcal{T}$. Triangulations in this family consist of only one type of obtuse triangles, numbered as shown in Figures 12 and 13. We denote α_i, α_j and α_k as the coefficients corresponding to the diamond schemes built repectively with the axes x and z, with the axes x and w, and with the axes z and w.

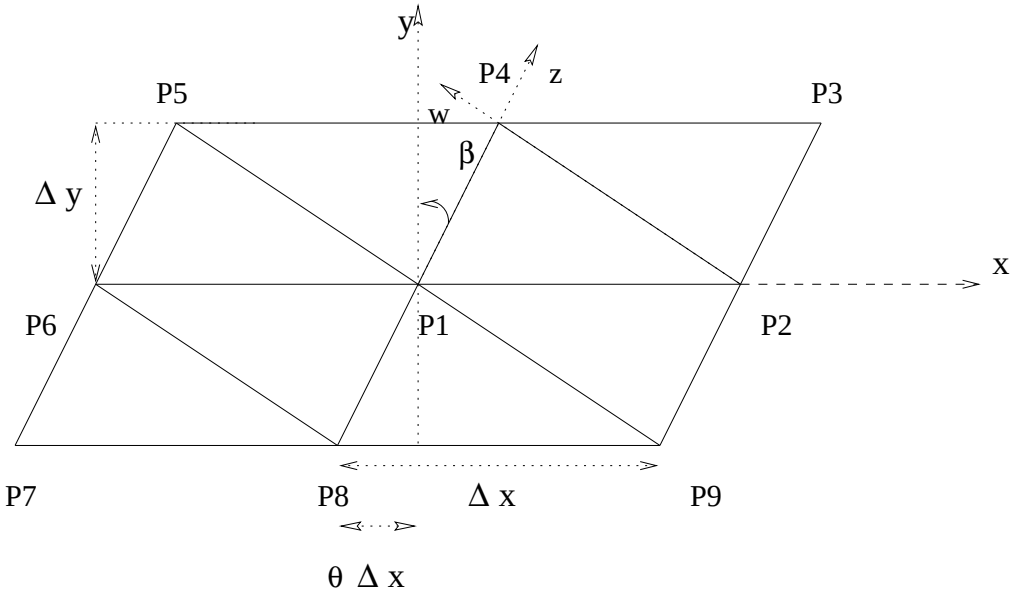

Figure 12: *Model triangulation $\mathcal{T}$.*

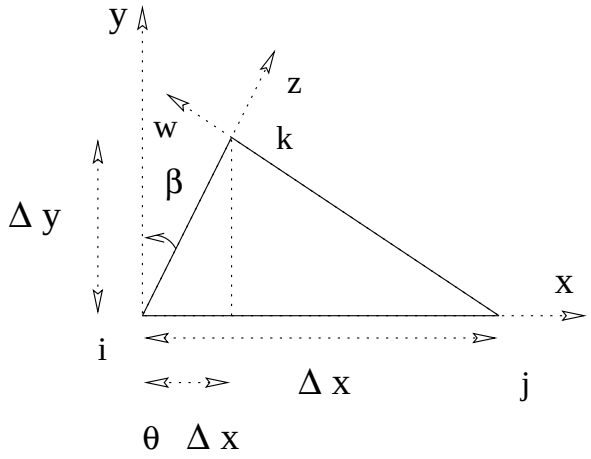

Figure 13: *Numerotation of vertices in a triangle of triangulation $\mathcal{T}$.*

The truncation error is obtained by computing the values of the mean normal vector applying Equation (49) and using a finite Taylor expansion around the point P1 of the values W(P_i), i = 2, 3, 4, 6, 7 and 9. We obtain the following result:

$$
\begin{aligned}
W_t \;=\; & -a && W_x \\
& -b && W_y \\
& +\frac{1}{2}\frac{\Delta x}{\Delta y}\left(\mid \vec{V}\cdot\vec{\eta}_{12}\mid \;+\; \mid \vec{V}\cdot\vec{\eta}_{14}\mid \;\theta^2 + \mid \vec{V}\cdot\vec{\eta}_{15}\mid (\theta-1)^2\right) && W_{xx} \\
& +\left(\mid \vec{V}\cdot\vec{\eta}_{14}\mid \theta + \mid \vec{V}\cdot\vec{\eta}_{15}\mid (\theta-1)\right) && W_{yx} \\
& +\frac{1}{2}\frac{\Delta y}{\Delta x}\left(\mid \vec{V}\cdot\vec{\eta}_{14}\mid \;+\; \mid \vec{V}\cdot\vec{\eta}_{15}\mid\right) && W_{yy} \\
& -\frac{1}{6}\frac{(\Delta x)^2}{\Delta y}\left((\vec{V}\cdot\vec{\eta}_{12}) + (\vec{V}\cdot\vec{\eta}_{14})\theta^3 + (\vec{V}\cdot\vec{\eta}_{15}))(\theta-1)^3\right) && W_{xxx} \\
& -\frac{1}{2}\Delta x\left((\vec{V}\cdot\vec{\eta}_{14})\theta^2 \;+\; (\vec{V}\cdot\vec{\eta}_{15})(\theta-1)^2\right) && W_{yxx} \\
& -\frac{1}{2}\Delta y\left((\vec{V}\cdot\vec{\eta}_{14})\theta \;+\; (\vec{V}\cdot\vec{\eta}_{15})(\theta-1)\right) && W_{yyx} \\
& -\frac{b}{6}(\Delta y)^2 && W_{yyy} \\
& +O\left((\Delta x)^3, (\Delta y)^3, \frac{(\Delta x)^4}{\Delta y}, \frac{(\Delta y)^4}{\Delta x}\right),
\end{aligned}
\tag{50}
$$

where

$$\vec{V}\cdot\vec{\eta}_{12} \;=\; a(\alpha_j+\alpha_i)\,\Delta y - b\,(\alpha_j\,(\theta-1)+\alpha_i\,\theta)\,\Delta x, \tag{51}$$

$$\vec{V}\cdot\vec{\eta}_{14} \;=\; a\,\alpha_k\,\Delta y + b\,(\alpha_i-\alpha_k\,(\theta-1))\,\Delta x, \tag{52}$$

$$\vec{V}\cdot\vec{\eta}_{15} \;=\; -a\,\alpha_k\,\Delta y + b\,(\alpha_j+\theta\alpha_k)\Delta x. \tag{53}$$

We now select three particular subsequences of the family of triangulation $\mathcal{T}$.

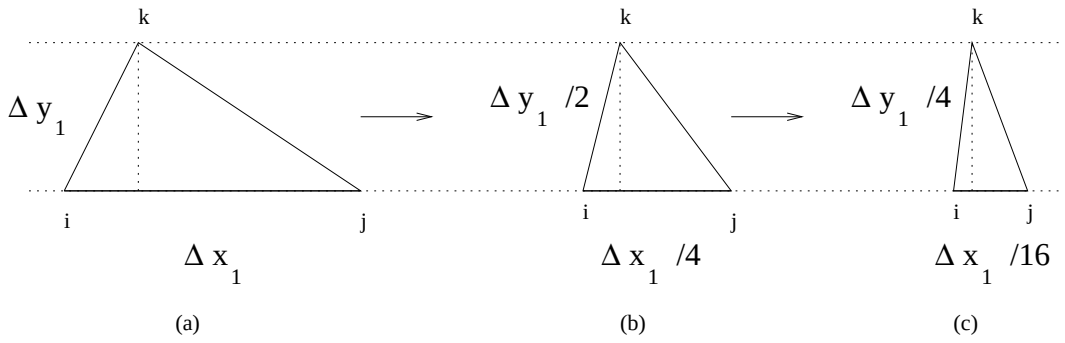

Figure 14: *Evolution of the shape of a triangle in triangulation $\mathcal{M}_n$: (a) triangle in $\mathcal{M}_1$, (b) triangle in $\mathcal{M}_2$, scale :2, (c) triangle in $\mathcal{M}_3$, scale :4.*

4.3 Stretched triangles with no obtuse angles

The mesh sequence $(\mathcal{M}_n)_n$ is defined by

$$\begin{aligned} \mathcal{M}_1 : \quad & \textit{Model triangulation } \mathcal{T} \textit{ shown in Figures 12 and 13.} \\ & \textit{The distance } \theta\,\Delta x \textit{ measures the non-orthogonality of the mesh.} \\ & \textit{We assume } 0 < \theta = const < \frac{1}{2}. \\ \mathcal{M}_n : \quad & (\Delta x)_n = \frac{\Delta x_1}{n^2}, \qquad (\Delta y)_n = \frac{\Delta x_1}{n}, \qquad \theta = const \ \blacksquare \end{aligned} \tag{54}$$

The triangulation sequence $(\mathcal{M}_n)_n$ is such that the larger is n, the more stretched is the mesh in the y direction, since

$$\lim_{n\to\infty} \frac{(\Delta x)_n}{(\Delta y)_n} = 0.$$

We observe that for n large, all triangles of $\mathcal{M}_n$ are *acute*.

The scheme is uniformly consistent on $\mathcal{M}_n$ for n tending to infinity only if in the truncation error (50) all terms tend to zero. This is verified if and only if the factors $\mid \vec{V} \cdot \vec{\eta}_{14} \mid$ and $\mid \vec{V} \cdot \vec{\eta}_{15} \mid$ defined in Equation (52) and (53) are small enough and in particular only if α_k, which corresponds to the diamond scheme relying on the two largest sides, is smaller

than $\dfrac{\Delta x}{\Delta y^2}$. Thus, we obtain the following necessary condition for consistency :

$$\alpha_k \;=\; o\left(\frac{\Delta x}{\Delta y^2}\right). \tag{55}$$

In this particular case, due to (54), the remainder, estimated as a $O\left((\Delta x)^3, (\Delta y)^3, \dfrac{(\Delta x)^4}{\Delta y}, \dfrac{(\Delta y)^4}{\Delta x}\right)$, tends to zero with n.

It is interesting to introduce the following definition of the aspect ratio of a triangle:

Definition:
We shall think of the aspect ratio of a given triangle as the ratio of its largest side divided by its smallest altitude.

We observe that the aspect ratio r'_n of mesh $\mathcal{M}_n$ satisfies:

$$r'_n \sim \frac{\Delta y}{\Delta x}.$$

Similarly, the largest altitude in triangles of $\mathcal{M}_n$ is of the same order as the largest side. Therefore, statement (55) can be written in the following general manner :

$$\alpha_k \;=\; o\left(\frac{1}{\text{largest side} \times r'_n}\right). \tag{56}$$

4.4 Stretched triangles with obtuse angles (1)

We consider now an obtuse stretched context $(\mathcal{N}_n)_n$ that is defined by

$$\begin{aligned}
&\mathcal{N}_1 : \quad \textit{Model triangulation } \mathcal{T} \textit{ shown in Figures 12 and 13.}\\
&\qquad\quad \textit{The angle } \beta = (\vec{z}, \vec{y}) \textit{ is kept constant;}\\
&\qquad\quad \textit{it can be either positive or negative and } -\frac{\pi}{2} < \beta < \frac{\pi}{2}.\\
&\mathcal{N}_n : \qquad (\Delta x)_n = \frac{\Delta x_1}{n}, \qquad (\Delta y)_n = \frac{\Delta y_1}{n^2}. \quad \blacksquare
\end{aligned} \tag{57}$$

The evolution of a triangle in the triangulation sequence $(\mathcal{N}_n)_n$ is given in Figure 15.

The triangulation sequence $(\mathcal{N}_n)_n$ is such that the larger is n, the more stretched is the mesh in the x direction, since

$$\lim_{n\to\infty} \frac{(\Delta y)_n}{(\Delta x)_n} = 0.$$

Let us examine the above truncation analysis; as for the above section, the remainder again tends to zero with n. We account for the following relation:

$$\theta = \frac{\Delta y}{\Delta x} \tan \beta, \tag{58}$$

which allows us to deduce that the scheme is uniformly consistent with regard to the stretching of the mesh only if in the truncation error all terms tend to zero. This is verified only if the factors $\mid \vec{V} \cdot \vec{\eta}_{12} \mid$ and $\mid \vec{V} \cdot \vec{\eta}_{14} \mid$ are small enough, that is if α_i is smaller than $\frac{\Delta y}{(\Delta x)^2}$. Thus, we derive the following necessary condition for consistency :

$$\alpha_j \;=\; o\left(\frac{\Delta y}{\Delta x^2}\right). \tag{59}$$

We observe that the aspect ratio r'' of mesh $\mathcal{N}_n$ satisfies:

$$r''_n \;=\; \frac{\Delta x}{\Delta y}.$$

Similarly, the largest side in triangles of $\mathcal{N}_n$ are of the same order as Δx.

Therefore, Equation (59) can be written in the more general manner :

$$\alpha_j \;=\; o\left(\frac{1}{\text{largest side} \times r''_n}\right). \tag{60}$$

We observe that $\mathcal{N}_n$ may present obtuse angles but these obtuse angles are uniformly bounded (i.e. a maximum angle condition is satisfied). We recall that, for the usual Galerkin method, assuming a maximum angle in the triangulation sequence is the poorest standard one. It is thus interesting to examine some examples for which this basic assumption is not verified.

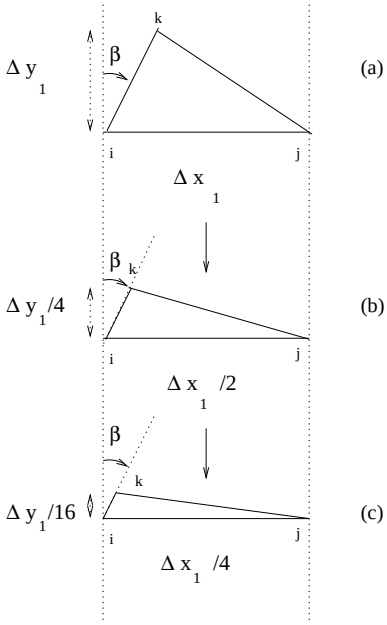

Figure 15: *Evolution of the shape of a triangle in triangulation $\mathcal{N}_n$: (a) triangle in $\mathcal{N}_1$, (b) triangle in $\mathcal{N}_2$, scale :2, (c) triangle in $\mathcal{N}_3$, scale :4.*

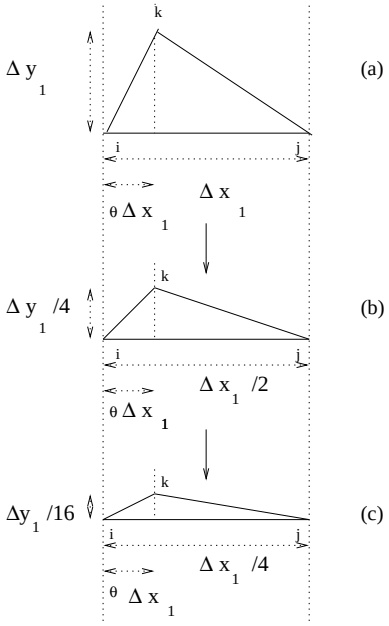

Figure 16: *Evolution of the shape of a triangle in triangulation $\mathcal{P}_n$: (a) triangle in $\mathcal{P}_1$, (b) triangle in $\mathcal{P}_2$, scale :2, (c) triangle in $\mathcal{P}_3$, scale :4.*

4.5 Stretched triangles with obtuse angles (2)

The mesh sequence $(\mathcal{P}_n)_n$ is defined by

$$\begin{aligned}
\mathcal{P}_1: &\quad \text{Model triangulation } \mathcal{T} \text{ shown in Figures 12 and 13.} \\
&\quad \text{The distance } \theta\,\Delta x \text{ measures the non-orthogonality of the mesh.} \\
&\quad \text{We assume } 0 < \theta = const < \frac{1}{2}. \qquad (61) \\
\mathcal{P}_n: &\qquad (\Delta x)_n = \frac{\Delta x_1}{n}, \qquad (\Delta y)_n = \frac{\Delta y_1}{n^2}. \blacksquare
\end{aligned}$$

The evolution of a triangle in the triangulation sequence $(\mathcal{P}_n)_n$ is given in Figure 16.

The triangulation sequence $(\mathcal{P}_n)_n$ is such that the larger is n, the more stretched is the mesh in the x direction, since

$$\lim_{n\to\infty} \frac{(\Delta y)_n}{(\Delta x)_n} = 0.$$

Moreover, no maximum angle condition is satisfied.

The truncation error in this context is again given by (50). On this triangulation sequence $\mathcal{P}_n$ the terms with $\frac{(\Delta x)_n}{(\Delta y)_n}$ *always* bring *inconsistency*.

4.6 Synthesis: Elementwise anisotropy

In order to avoid a local numerotation of the triangles and to make the method more practical, from now on, we call *schemes DS, DM and DL* the diamond schemes relying on the vertices opposite respectively the smallest, the medium and the largest side of the triangle. We denote α_{DS}, α_{DM} and α_{DL} as the coefficients related respectively to the schemes DS, DM and DL.

The two first contexts of triangulation sequence did satisfy a uniform majoration of the largest angle, because either all angles where acute or the largest angle was held constant or smaller than a given angle; the third analysis seems to show that a maximum angle assumption remains a minimal one, which we cannot today get rid of.

The results of the analysis of Sec. 4.3 and 4.4 can be synthetised as follows:

We first remark that for the acute triangulation sequence, the coefficient α_k in Equation (56) corresponds to the diamond scheme along the two largest sides of each triangle, and so does the coefficient α_j in Equation (60) of the first obtuse triangulation sequence, then both necessary conditions concern the DS scheme, that is:

Lemma 4.1 *A necessary condition for a barycenter of the three diamond schemes to be consistent for any family of mesh, is that in case of high stretching the coefficient of the diamond version relying on largest sides be small enough according to the following rule:*

$$\alpha_{DS} \;=\; o\left(\frac{1}{\textit{largest side} \times r_n}\right), \tag{62}$$

where r_n denotes the aspect ratio.

It is clear that the schemes DL and DM are two admissible choices as far as consistency on regular meshes is concerned. But for non uniform meshes, the non regular switch between sides, for example on nearly isosceles triangles, may induced some irregularity in the resulting approximation. We thus need to specify an appropriate *smooth barycenter*.

With this end in view, we make an inventory of the following desired properties:

- **indispensable criteria**

  (i) If there is a right angle then choose the two sides other than the hypothenuse.

  (ii) If a triangle is isosceles the symmetry should be respected : same weight on the two symmetric sides.
  This implies that for equilateral triangles the weight should be one third on each side.

  (iii) The weight should be smooth.

  We note that (ii) ensures that the ambiguity in choosing the smallest between two symmetric sides has no influence on the resulting scheme.

- **additional criteria for stretched mesh**

  We need to choose a strategy in case of an obtuse angle. We keep the same strategy as for a right angle.

  (i)' if there is an obtuse angle then choose the two sides other than the largest side.

An example:
It is natural to seek obtuseness indicators satisfying:

$$\begin{array}{c} \beta_S = 0 \text{ if } \hat{S} \geq \frac{\pi}{2}, \\ \beta_M = 0 \text{ if } \hat{M} \geq \frac{\pi}{2}, \\ \beta_L = 0 \text{ if } \hat{L} \geq \frac{\pi}{2}. \end{array} \tag{63}$$

where $\hat{S}$, $\hat{M}$ and $\hat{L}$ are respectively the angles opposite to sides S, M and L (see Figure 17).

We define then the following coefficients:

$$\begin{array}{c} \overline{\alpha_{DS}} = \beta_M \, \beta_L, \\ \overline{\alpha_{DM}} = \beta_S \, \beta_L, \\ \overline{\alpha_{DL}} = \beta_S \, \beta_M. \end{array} \tag{64}$$

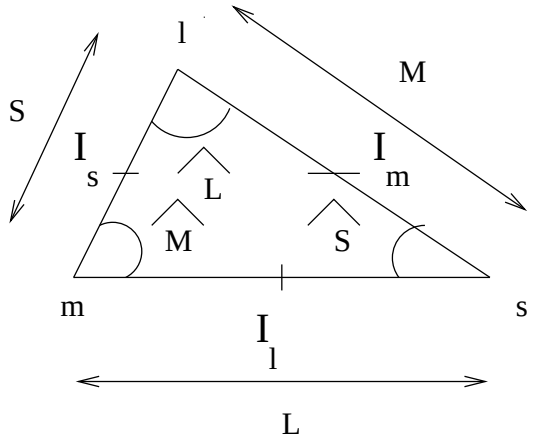

Figure 17: *Notation in a triangle: S, M and L are the lengths of respectively the smallest, medium and largest side. s, m and l are the vertices opposite to respectively the smallest, medium and largest side. $\hat{S}$, $\hat{M}$ and $\hat{L}$ are the angles opposite to respectively the smallest, medium and largest side. I_s, I_m and I_l are the middle points of respectively the smallest, medium and largest side.*

The choice of β satisfying (63) enables us to have $\alpha_{DL} = 0$ if the angle $\hat{S}$ or the angle $\hat{M}$ is obtuse. The same properties hold for α_{DS} and α_{DM}.
We normalize the coefficients of (64):

$$\begin{aligned}
\alpha_{DS} &= \frac{\overline{\alpha_S}}{\overline{\alpha_S} + \overline{\alpha_M} + \overline{\alpha_L}}, \\
\alpha_{DM} &= \frac{\overline{\alpha_M}}{\overline{\alpha_S} + \overline{\alpha_M} + \overline{\alpha_L}}, \\
\alpha_{DL} &= \frac{\overline{\alpha_L}}{\overline{\alpha_S} + \overline{\alpha_M} + \overline{\alpha_L}}.
\end{aligned} \tag{65}$$

We easily verify that if $\hat{S}$ is obtuse, α_M and α_L are vanishing, so that **(i)'** is satisfied.

Let us introduce a method for establishing β values which satisfy (63).

The detection of right and obtuse angles is (rather) smoothly detected via the Pythagoras formula as follows:

$$\begin{array}{l} \beta_S = f(\text{Max}(0, L^2 + M^2 - S^2)), \\ \beta_M = f(\text{Max}(0, S^2 + L^2 - M^2)), \\ \beta_L = f(\text{Max}(0, S^2 + M^2 - L^2)). \end{array} \tag{66}$$

where f is a positive increasing function, $f(x)$ is vanishing for $x = 0$, and S, M, L are respectively the lengths of the smallest, medium and largest sides.

We have managed the satisfaction of the consistency for obtuse angles; let us now analyze it for the *acute* family of meshes: we will compute the coefficient α_{DS}, α_{DM} and α_{DL} in this context. In the case $f(x) = x$, Equation (65) can be written as

$$\left\{ \begin{array}{lcl} \alpha_{DS} & = & \dfrac{1}{\tan(\hat{M})\,\tan(\hat{L})}, \\ \alpha_{DM} & = & \dfrac{1}{\tan(\hat{S})\,\tan(\hat{L})}, \\ \alpha_{DL} & = & \dfrac{1}{\tan(\hat{S})\,\tan(\hat{M})}. \end{array} \right. \tag{67}$$

We derive that for this choice of f, the scheme defined in (49) satisfies the consistency necessary conditions (62). Note that for example the choice $f(x) = \sqrt{x}$ would not produce the consistency relation while $f(x) = x^2$ would. In practice we will take $f(x) = x$.

4.7 Relation to existing finite-volume schemes

The relation to existing finite-volume schemes is summarized in Table 1. Details are given in Appendix I.

The Barycentered Diamond (BD) scheme with coefficient (67) can be in fact identified as the Barth circumcenter method [4]. Therefore, we call this scheme, the BD$_{Barth}$ method. In the numerical tests we will show results for $f(x) = x^2$, we will refer to this method as the BD$_{\text{square}}$ method, and for $f(x) = \sqrt{x}$, we will refer to this method as the BD$_{\text{root}}$ method. It can be verified from (50)-(53) that BD$_{Barth}$ and BD$_{\text{square}}$ are consistent for stretching and that BD$_{\text{root}}$ is not.

Location of Point C	$(\alpha_{DS}, \alpha_{DM}, \alpha_{DL})$
Middle of $[S]$	(1, 0, 0)
Middle of $[M]$	(0, 1, 0)
Middle of $[L]$	(0, 0, 1)
Intersection of the medians	$\left(\frac{1}{3}, \frac{1}{3}, \frac{1}{3}\right)$
Circumcenter	$\left(\frac{1}{\tan(\hat{M})\,\tan(\hat{L})}, \frac{1}{\tan(\hat{S})\,\tan(\hat{L})}, \frac{1}{\tan(\hat{S})\,\tan(\hat{M})}\right)$

Table 1: *Example of equivalence between a given location of the point C used to build the finite-volume cell and barycenter coefficients used to build a scheme of the diamond family in the case of an acute triangle.*

5 Upwind formulation for CFD : MUSCL

Since we have shown that our scheme is a finite-volume one, we can derive a second-order accurate MUSCL extension.

Equation (10) can be written as,

$$Area(C_m)\, W_{m,t} + \sum_{\substack{n=1 \\ n \neq m}}^{N} \Phi^{centered}(W_m, W_n, \vec{\eta}_{mn}) = 0. \tag{68}$$

The extension of the Donor Cell formulation (12) to Euler equations consists in using a Riemann problem with W_m and W_n as left and right states and $\vec{\eta}_{mn}$ for defining the interface. We are now left with a one-dimensional problem which may be solved by a Godunov solver or an approximate Riemann solver like Roe's solver.

Equation (68) is replaced with

$$Area(C_m)\, W_{n,t} + \sum_{\substack{n=1 \\ n \neq m}}^{N} \Phi^{upwind}(W_m, W_n, \vec{\eta}_{mn}) = 0, \tag{69}$$

where $\Phi^{upwind}(W_m, W_n, \vec{\eta}_{mn})$ are the first-order numerical fluxes.

A second-order spatial accurate scheme for hyperbolic terms can be obtained using the MUSCL interpolation technique introduced by van Leer [22]. To reach the second-order accuracy the numerical fluxes are evaluated with extrapolated values W_{mn} and W_{nm} at the interface ∂C_{mn}. Thus, the function Φ remains the same, only its arguments are modified:

$$Area(C_m)\, W_{n,t} + \sum_{\substack{n=1 \\ n \neq m}}^{N} \Phi^{upwind}(W_{mn}, W_{nm}, \vec{\eta}_{mn}) = 0, \tag{70}$$

The quantities W_{mn} and W_{nm} are computed by

$$\begin{aligned} W_{mn} &= W_m + \frac{1}{2} \nabla W_{mn} \cdot m\vec{n}, \\ W_{nm} &= W_n + \frac{1}{2} \nabla W_{nm} \cdot n\vec{m}. \end{aligned} \tag{71}$$

A gradient centered at the middle of the edge $[mn]$ (see Figure 18) is defined by

$$(\nabla W)_{mn}^{centered} \cdot \vec{mn} = W_n - W_m, \tag{72}$$

and an upwind gradient is defined by

$$\begin{aligned} (\nabla W)_{mn}^{upwind} \cdot \vec{mn} &= \nabla W \mid_{T_{mn}} \cdot \vec{mn}, \\ (\nabla W)_{nm}^{upwind} \cdot \vec{nm} &= \nabla W \mid_{T_{nm}} \cdot \vec{mn}, \end{aligned} \tag{73}$$

where T_{mn} and T_{nm} are defined in Figure 18, and where $\nabla W \mid_{T_{mn}}$ is the finite element approximation of the gradient.

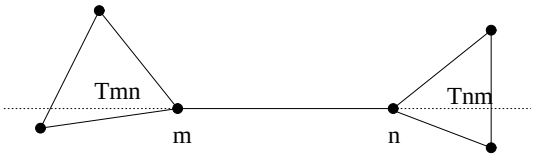

Figure 18: *Downstream and upstream triangle T_{mn} and T_{nm}.*

We can use a "β-scheme" which combines the centered and fully upwind gradient to obtain

$$\nabla W_{mn} \cdot \vec{mn} = (1 - \bar{\beta})(\nabla W)_{mn}^{centered} \cdot \vec{mn} + \bar{\beta}\,(\nabla W)_{mn}^{upwind} \cdot \vec{mn} \tag{74}$$

where $\bar{\beta}$ is the parameter of upwinding included in interval $[0, 1]$. In the test cases presented in the sequel, we took either $\bar{\beta} = \frac{1}{2}$ or $\bar{\beta} = \frac{1}{3}$.

The scheme described above is not monotone. It can introduce extrema which would not exist, particularly in the case of transonic and supersonic flows. To reduce the oscillations in the solution a LED slope-limiting procedure can be used as in [6]. In our test cases, we did not use limiters.

6 The linearity preservation property

We are now concerned by the local consistency of the second order versions (centered and upwind) of the *diamond* scheme. We will consider both the optimal consistency for stationary solutions on cartesian meshes, and a consistency on unstructured non-stretched triangulations. For formally second order schemes, the local consistency can be obtained with the

so-called *Linearity preservation* properties [14] [4] [21].
We first review two properties of linearity preservation in the context of the scalar linear equation (11) ; we then consider the ability of the *diamond* scheme to be exact for affine functions.

Definitions

The *diamond* scheme (26)-(27)-(25) writes in the following fluctuation-splitting (or distributive) form (see also section 3.5):

$$\sum_{n=1}^{N} w_{n,t} \int_{\Omega} \Psi_m^C \varphi_n d\Omega + \sum_{T;x_m \in T} \phi_m^T = 0, \qquad \forall m = 1,..,N, \tag{75}$$

where the fluctuation at node m writes $\phi_m^T = \int_{C_m \cap T} \vec{V} \cdot \vec{\nabla}_h(\pi_h w) d\Omega$ (π_h is the P_1-Lagrange interpolation operator). We have $\phi_m^T = \beta_m^T \Phi^T$ where Φ^T is the total fluctuation. The cell C_m is defined as in Section 3 (see (14) for the test functions and (25) for the definition of $\vec{\nabla}_h$) and we have shown that the spatial term of (75) is in fact independent of the choice of C_m. The conservativity of the scheme, in the fluctuation splitting sense, is given by: $\sum_{m=i,j,k} \phi_m^T = \Phi^T$ and is equivalent to (19).

Let us recall two well-known properties of polynomial preservation:

(i) A scheme is said to be linear preserving (*LP*) if the spatial approximation $\mathcal{L}_h$ is exact for linear functions [4, 14]:

$$(\mathcal{L}_h p)_m = \mathcal{L} p, \qquad \forall m = 1,..,N, \quad \forall p \in P_1(\Omega).$$

A more particular notion of linear preserving is the following:

(ii) A *fluctuation splitting* scheme is said to be linear preserving if a linear *stationary* solution of (11) is also a solution of the scheme, or equivalently if for $p \in P_1(\Omega)$ such that $\vec{V} \cdot \vec{\nabla} p = 0$ (then $\Phi^T(p) = Area(T) \vec{V} \cdot \vec{\nabla} p = 0$), we have:

$$\phi_m^T(p) = \beta_m^T(p) \Phi^T(p) = 0, \quad \forall m = i,j,k.$$

This is equivalent to saying that the coefficient β_m^T is bounded when Φ^T tends to zero. If the scheme is linear, one can show that the scheme is linear preserving in this sense if and only if the coefficients= β_m^T is independent of p [21]. In the sequel, we call this property written in the fluctuation splitting form, the property *LP-FS*.

Consistency of *LP* and *LP-FS* schemes

For stationary solutions, the *LP-FS* schemes (e.g. SUPG, PSI,...) are consistent and have a second order truncation error *on cartesian meshes* with a uniform choice of diagonals (Figure 7). For general solutions, the *LP* property (i) provides a local consistency of order one on unstructured meshes, the only conditions on the mesh being the regularity (in the finite element sense) and a local quasi-uniformity [14].

Consistency of the *diamond* scheme

We can highlight the following properties of the diamond scheme:

We first consider the *central differenced* diamond scheme equivalent to the scheme of Sidilkover (47). This scheme is not *LP-FS* in the general case, since if $\Phi^T = 0$ (which gives $R_\xi + R_\eta = 0$), this does not imply that the distributed fluctuations $\phi_m^T = 0$ (i.e. $R_\xi = R_\eta = 0$). However, it is *LP-FS* in some particular cases, for example if one of the two edges chosen for the diamond derivatives is colinear to $\vec{V}$ (see (48)).
The barycentered formulation with equal coefficients (i.e. the median dual scheme or the Galerkin scheme) is *LP-FS* on any triangulations.

We now consider the *upwind* diamond schemes. A *LP* version of the MUSCL scheme of Section 5 (70-71) can be obtained in the following manner: we can replace Equation (70) by the following scheme:

$$Area(C_m)\, W_{n,t} + \sum_{\substack{n=1 \\ n \neq m}}^{N} \int_{\Gamma_{mn}} \Phi^{upwind}(W^-(\vec{x}), W^+(\vec{x}), \vec{\eta}_{mn}(\vec{x})) = 0, \qquad (76)$$

where Γ_{mn} is the interface defined by the normals $\vec{\eta}_{mn}$ and $W^-(\vec{x}), W^+(\vec{x})$ are the left and right values of the reconstruction on the interface. If the reconstruction and the numerical integration of the flux are exact for affine functions, then the above scheme is *LP* if we choose C_m as the cell defined by the normals $\vec{\eta}_{mn}$. This property for the reconstruction is usually called the *k-exactness* property [4] (here for $k = 1$). For the numerical integration, we can consider a Gauss quadrature ; in this case, we should consider the values of the reconstructions in the middle point of each portion of the interface Γ_{mn}^l ($l = 1, 2$), with normal $\left(\eta_{mn}^T\right)_l$.

7 Some numerical illustrations

Let us first evaluate with a very simple example how large the difference can be between a scheme that is consistent with stretching, and a scheme that is not, even for rather mild stretching. We consider the unsteady concentration cone test case, described for example in [9].
Then, we consider several easy academic cases in simple geometries such as flow around a circular cylinder. These test cases have already been widely investigated which enables us to compare our results with existing ones. All presented results are obtained with the Roe scheme and no limiters are used.
Finally, improvements brought by the diamond scheme in case of quasi-cartesian meshes is illustated on a flow in a booster combustion chamber.

In the sequel we will consider the five following schemes:

- **a.** The Finite Volume scheme with median cells; we will refer to "Median scheme" for both the first-order version and its extension to the second order.
- **b.** The diamond scheme with a barycenter with $f(x) = x$ (the function $f(x)$ was introduced in (66)), we refer to BD_{Barth} scheme.
- **c.** The diamond scheme with a barycenter with $f(x) = x^2$, we refer to BD_{square} scheme.
- **d.** The diamond scheme with a barycenter with $f(x) = \sqrt{x}$, we refer to BD_{root} scheme.

7.1 Unsteady flow: rotation of a conical spot

This is a very classical test for evaluating unsteady advection schemes (see for example [10]).

The equation to be solved is:

$$\left\{ \begin{array}{rcll} W_t + div(\overrightarrow{V}W) & = & 0 & in\ \Omega =]0,1[^2 \\ W_0(x,y) & = & \max(1, 2 - 5\sqrt{(x-0.25)^2 + (y-0.5)^2}) & \\ W(x,y) & = & 1 & on\ \partial\Omega \end{array} \right. \quad (77)$$

with the advection speed $\overrightarrow{V} = \pi \begin{pmatrix} y - 0.5 \\ 0.5 - x \end{pmatrix}$.
The solution is observed after a complete turn (t=2s).

Two schemes are examined: the first one is the Median scheme, the second one is the BD_{Barth} scheme.
Time integration relies on the corresponding areas. Third order version of both schemes are considered ($\overline{\beta} = 1/3$, no limiters, Runge-Kutta 3 time stepping).
With a 31x31 cartesian mesh, the BD_{Barth} scheme produces a rather good solution (Figure 21). With a division by a factor 5 of Δy, we observe an impressive improvement (Figure 22). Conversely, the Median scheme gives a less good but acceptable solution on a 31x31 mesh (Figures 19) , and a notably less good solution on the 31x155 one, which shows a quite undesirable manifestation of the inconsistency for stretched meshes (Figure 20).

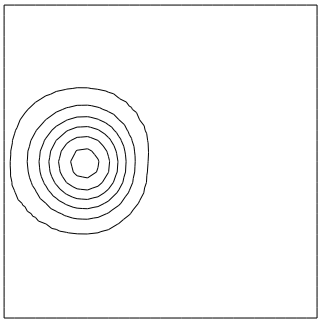

Figure 19: *Rotation of a conical spot:* `Median` *scheme. Solution for the* `31×31` *node mesh.*

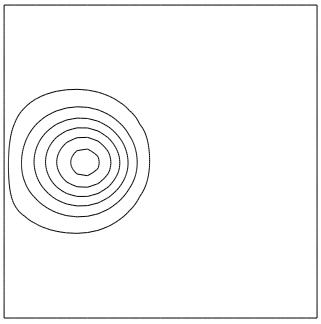

Figure 20: *Rotation of a conical spot:* `Median` *scheme. Solution for the* `31×155` *node mesh.*

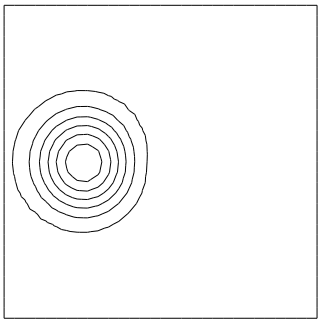

Figure 21: *Rotation of a conical spot:* BD_{Barth} *scheme. Solution for the* `31×31` *node mesh* .

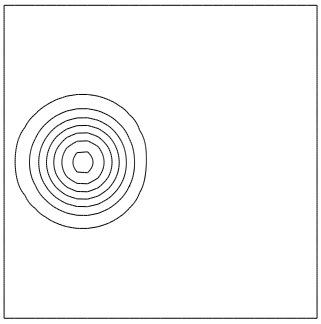

Figure 22: *Rotation of a conical spot:* BD_{Barth} *scheme. Solution for the* `31×155` *node mesh.*

7.2 Flow around a circular cylinder

We turn now to a steady flow simulation. The pathological behaviour of median cells was already noted by T. Barth [4]. We give here a simple and demonstrative example.

The flow is inviscid and the Mach number at infinity is equal to 0.38. The flow is steady. Experiments have been performed on two meshes of different coarsening and stretching:
i) a structured non-stretched mesh of 1088 vertices (see Figures 23 and 25),
ii) a structured stretched mesh of 2112 vertices (see Figures 24 and 26). The maximum aspect ratio near the wall is 20.

On both meshes, the solutions obtained with the Median scheme are shown in Figures 27 and 28, and the solutions obtained with the BD_{Barth} method are shown in Figures 29 and 30.

The results on the non-stretched mesh show that for quasi-cartesian meshes, and even in the absence of stretching, the BD_{Barth} method enables a better accuracy; this is indicated in particular by a better symmetry of Mach contours between the front and rear parts of the cylinder.

On the stretched mesh the solution obtained with the Median method at first-order spatial accuracy is totally degraded while the solution obtained with the BD_{Barth} method is acceptable. One could believe that second-order accuracy would improve the results obtained with the Median scheme. This is not the case; indeed, at second-order spatial accuracy, two large vortices appear behind the cylinder and the steady state cannot be reached. With the diamond method the steady state solution is close to the solutions obtained with the non-stretched mesh but again with a noticeable improvement.

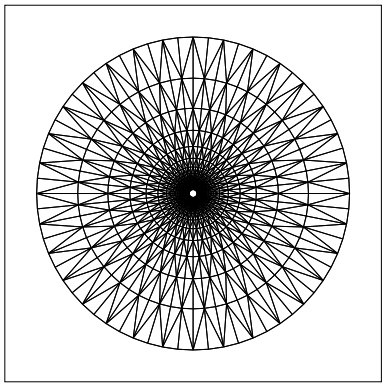

Figure 23: *Non-stretched mesh with 1088 vertices.*

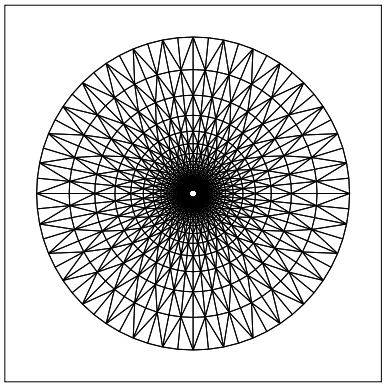

Figure 24: *Stretched mesh with 2112 vertices.*

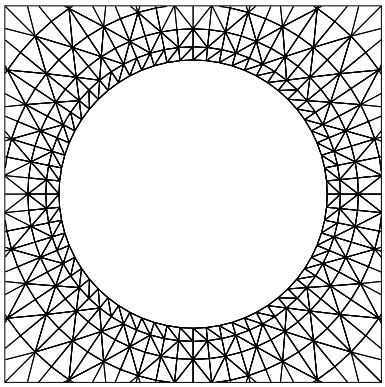

Figure 25: *Zoom of the mesh with 1088 vertices.*

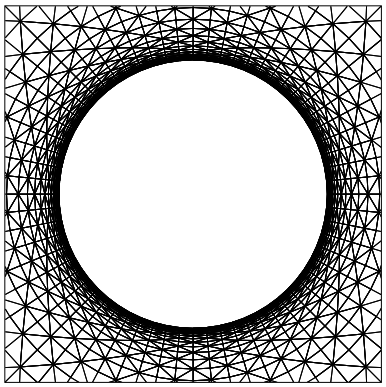

Figure 26: *Zoom of the mesh with 2112 vertices; the maximum aspect ratio is 20.*

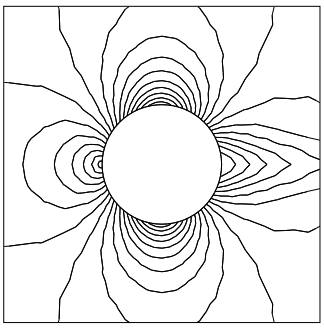

Figure 27: *Mach contours,* $M_\infty = 0.38$*,* 2^{nd}*-order accuracy,* `1088` *vertex mesh,* `median` *cells. Isovalues:* $0 : 0.05 : 1$.

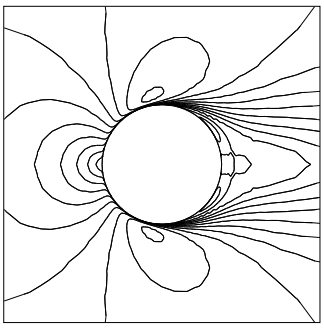

Figure 28: *Mach contours,* $M_\infty = 0.38$*,* 1^{st}*-order accuracy,* `2112` *vertex mesh,* `median` *cells. Isovalues:* $0 : 0.05 : 1$.

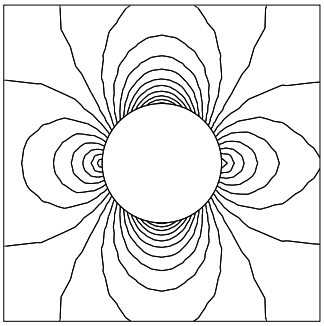

Figure 29: *Mach contours,* $M_\infty = 0.38$*,* 2^{nd}*-order accuracy,* `1088` *vertex mesh,* `Barth` *cells. Isovalues:* $0 : 0.05 : 1$.

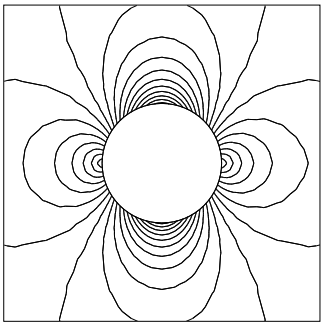

Figure 30: *Mach contours,* $M_\infty = 0.38$*,* 2^{nd}*-order accuracy,* `2112` *vertex mesh,* `Barth` *cells. Isovalues:* $0 : 0.05 : 1$.

7.3 Flow in a booster combustion chamber

Many combustion engines involve important acoustic effects taking place in their combustion chambers and coupling with vortex shedding. The geometries of these chambers are generally rather complicated and may motivate the use of unstructured "generalist" flow codes.
However, theses codes should not involve much internal viscosity since acoustics and vortices play an important role.
For example, a powder rocket may present a cavity with a starshaped section best described with triangulations. But tetrahedra/triangles-relying upwind approximations contain generally a big amount of internal viscosity.

We propose here a 2-D test that aims at qualifying the BD_{Barth} scheme as involving a low internal viscosity so that it will be able to compute this kind of flow.
We present the computation of the flow in a 2D geometry related to a booster of the launcher ARIANE V referenced in litterature as the C1 test case. This flow is transonic and unsteady; the Mach number varies between 0.05 and 1.7. In this chamber (Figure 31) the flow of gas through the burning powder is driven through the cavity and the inlet S. The right part of the cavity will be occupied by a large vortex and small vortices will be shed from left to right with coupling with acoustics. Several frequencies have been observed in other computations (2600 Hz, 3500Hz).

The propeller is modelled by a simplified and fixed geometry which is discretized with a mesh involving 9868 nodes (318×31) and made of triangles that are nearly isosceles and with a right angle. We thus again are examining the adequation of the new scheme to quasi-cartesian meshes as analysed in Section 3.3. We consider that the injected propergol is a perfect gas. The flow is computed with the compressible Euler equations using the different schemes. Time advancing is calculated by the 3-stage Runge Kutta time advancing by taking a CFL number equal to 1 . The boundary conditions are the following (see Figure 31) :

- We apply $\vec{V} \,.\, \vec{n} \,=\, 0$ on the sides $G1$, $G2$ and $G3$.
- The condition on D is a "discharge condition" which imposes that $Q \,\geq\, 0$ is constant perpendicular to the wall with a given temperature T_b which can be written as :

$$\rho \vec{V} \,=\, -\, Q \, \vec{n} \;\;,\;\; T \,=\, T_b \,. \tag{78}$$

  where $\vec{n}$ is the outside normal to the wall.
- On S, we have a supersonic outlet condition.

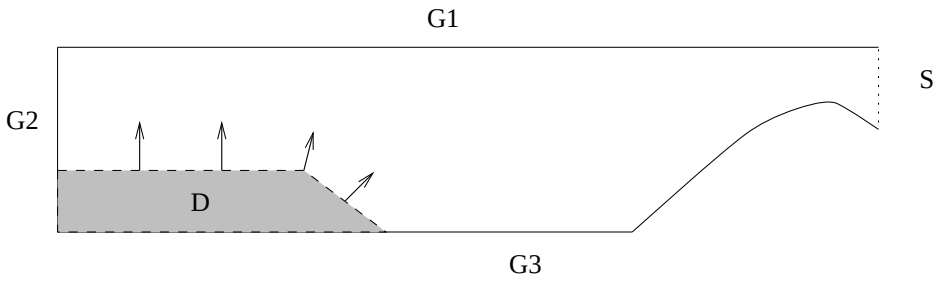

Figure 31: *C1 test case: hot gases are blown from the boundary of the powder block D, and will finally go out through the nozzle S.*

This test has been studied in details in [5]. The expected exact answer is a quasi periodic flow with a quasi constant amplitude of fluctuation.

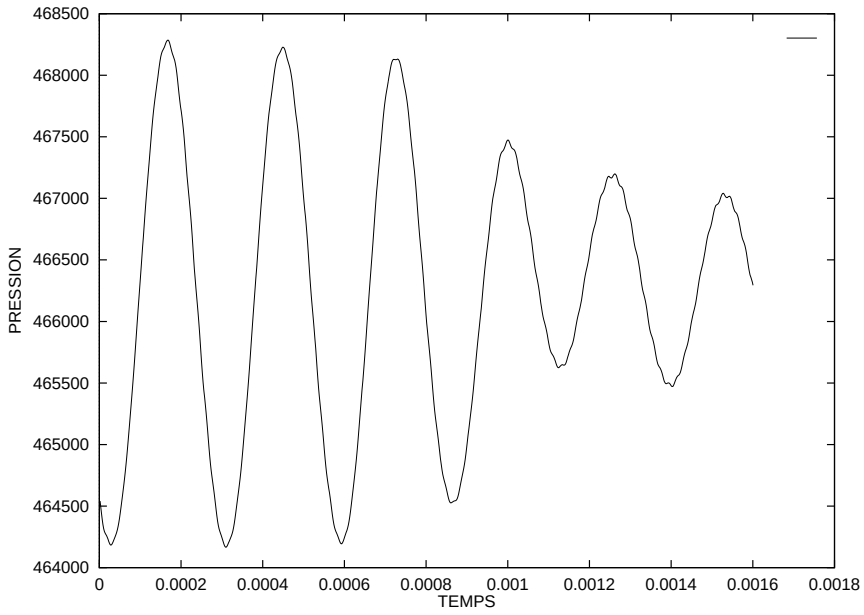

Figure 32: *C1 test case: Mediane scheme. Pressure at a point on the front combustion chamber. The main mode is spuriously damped (rather astonishingly a second one appears).*

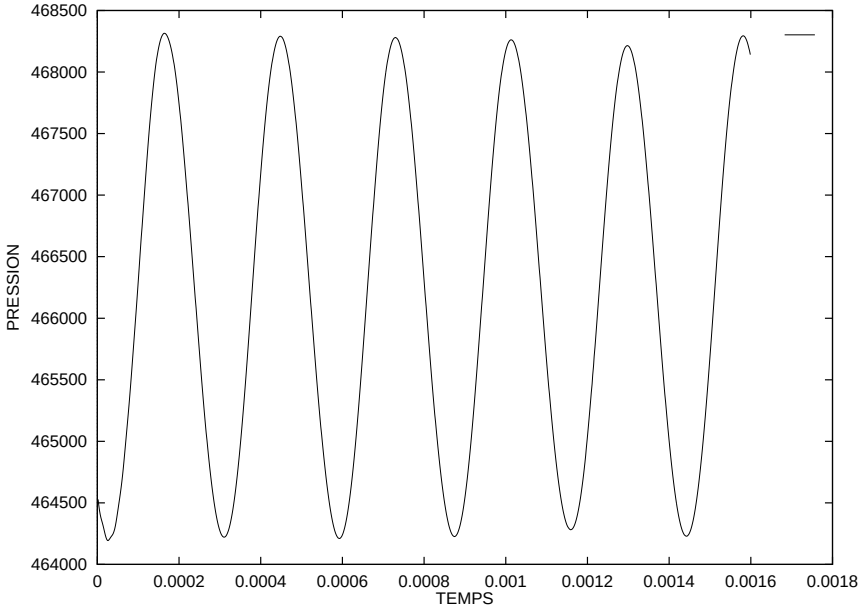

Figure 33: *C1 test case: BD$_{Barth}$ scheme. Pressure at a point on the front combustion chamber. The main mode keeps its amplitude.*

It was in particular observed that a very poor result was obtained with the Median method, with the "best option" $\overline{\beta} = 1/3$ on a regular mesh of 318×31 nodes. The scheme involves a rather large internal viscosity in many mesh directions and produce fastly damped fluctuation converging finally to a steady solution (Figure 32).

Applying the BD$_{Barth}$ scheme results in a considerable reduction of this viscosity and allows a good prediction of the expected vortices (Figure 33). The results show that the average pressure on the front combustion chamber is equal to about 466250 Pa. From the results of Figure 33, the acoustic frequency can be evaluated as about 3500 Hz. Solutions obtained with variants of the BD scheme are presented in Figure 34.

8 Concluding remarks

This work has focused on the consistency question for stretched meshes when a particular class of *upwind* schemes is applied. These schemes apply on triangulations, with unknowns

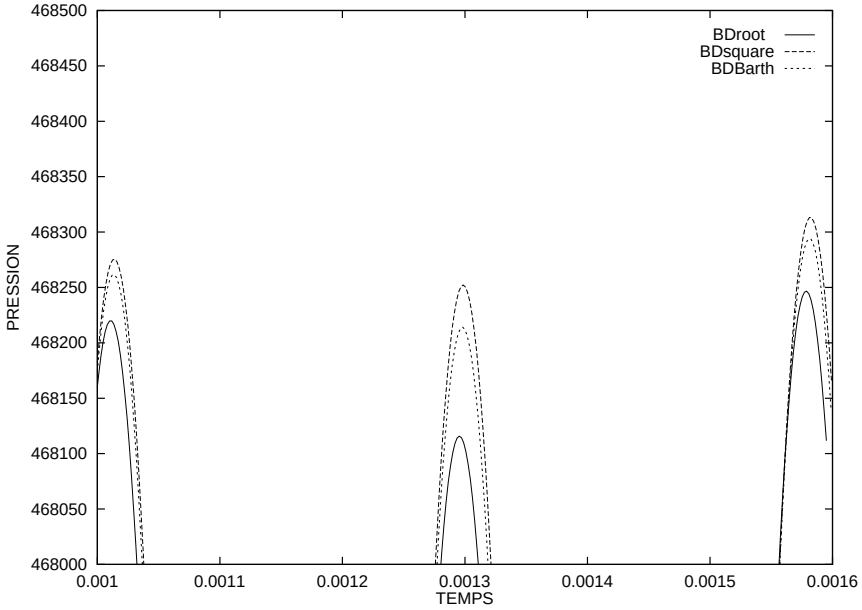

Figure 34: *C1 test case: Pressure at a point on the front combustion chamber. This is a zoom of Figure 33 with three curves, to illustrate the variations induced by three possible choices of the function f(x) (cf. (66)). The option* $f(x) = x^2$ *(*BD_{square}*) is slightly better than* $f(x) = x$ *(*BD_{Barth}*);* $f(x) = \sqrt{x}$ *(*BD_{root}*) gives the worst result.*

located on vertices.

For this purpose, we gather and complete a global view of several modern approximation schemes: finite-element, finite-volume, distribution schemes.
A family of upwind Godunov-type finite-volume schemes is then extracted for investigating which subset may satisfy the proposed criterion of *consistency in stretching*.
In order to have *necessary conditions*, we performed a truncation analysis for several typical sets of regular meshes and proposed some design criteria for building better schemes.
We show in particular that the Barth cell allows the corresponding finite-volume scheme to satisfy the proposed criterion.
Some numerical experiments illustrate that our point of view is reasonable.
While bringing some answers, this paper let many questions pending.

Firstly, a general analysis for unstructured stretched meshes is missing. It would be interesting to investigate under which conditions these schemes would be convergent for stretched meshes.

Secondly, although we have presented several different points of view in the derivation of the presented schemes, the extension to other types of elements is not straightforward: which strategy will be adequate for quadrilaterals, for tetrahedra, etc.

Answers to these kinds of questions are of paramount interest for design of new schemes for modern Reynolds-averaged Navier-Stokes calculations on unstructured meshes involving stretching and possibly anisotropic adaption devices.

9 Acknowledgments

We thank R. Carpentier for his kind help in the implementation of the booster test case, and J. Francescatto and D. Sidilkover for fruitful discussions. This paper is part of the first author's thesis work which has been jointly supported by CNES and RENAULT.

References

[1] R. Abgrall and K. Mer. Un théorème de type Lax-Wendroff pour les schémas distributifs. Technical Report 98015, Université de Bordeaux, 1998.

[2] P. Arminjon, A. Dervieux, L. Fezoui, H. Steve, and B. Stoufflet. Non-oscillatory schemes for multidimensional Euler calculations with unstructured grids, Nonlinear hyperbolic equations. *Theory, numerical methods and applications*, Ballmann & Jeltsch eds., pp. 1-10, Notes on Numerical Fluid Mechanics, 24, Vieweg, Braunschweig, 1989.

[3] K. Baba and M. Tabata. On a conservative upwind finite element scheme for convective diffusion equations. *R.A.I.R.O. Analyse numérique/Numerical Analysis*, 15:3 – 25, 1981.

[4] T. Barth. Aspects of unstructured grids and finite-volume solvers for the Euler and Navier-Stokes equations. Technical Report 787, AGARD, 1992. Also in von Karmann Institute Lecture Series, 1995.

[5] R. Carpentier. *Approximation et analyse numérique d'écoulements instationnaires. - Application à des instabilités tourbillonnaires.* PhD thesis, Université de Nice-Sophia-Antipolis, 1995.

[6] C. Debiez. *Approximation et linéarisation d'écoulements aérodynamiques instationnaires*. PhD thesis, Université de Nice Sophia-Antipolis, 1996.

[7] H. Deconinck. Upwind methods and multidimensional splittings for the Euler equations. *Computational Fluid Dynamics*, 1991. In von Karmann Institute Lecture Series 1991-01.

[8] A. Dervieux, L. Fezoui, and F. Loriot. On high resolution extensions of Lagrange-Galerkin finite-element schemes. Research Report 1703, INRIA, 1992.

[9] A. Goudjo. *Singularités d'arêtes en thermique et résolution de quelques problèmes hyperboliques*. PhD thesis, Université de Nice-Sophia Antipolis, 1990.

[10] P. Gresho and R.L. Lee and R.L. Sani. Advection dominated flows with emphasis on the consequence of mass-lumping. *Finite Elements in Fluids*, vol. 3, 1979. - Proceedings of the Second Int. Conf. on F.E.M. in flow problems (Santa Margherita Ligure, Italy, 1976).

[11] T.J.R. Hughes and M. Mallet. A new finite element formulation for computational fluid dynamics: Iii. the generalized-capturing operator for multidimensional advective-diffusive systems. *Computer Methods in Applied Mechanics and Engineering*, 58:305 – 328, 1986.

[12] C. Kasbarian, M.-P. Leclercq, M. Ravachol, and B. Stoufflet. Improvements of upwind formulations on unstructured meshes. In *Fourth International Conference on Hyperbolic Problems*, 363 – 368, 1992.

[13] D.J. Mavriplis and A. Jameson. Multigrid solution of the Navier-Stokes equations on triangular meshes. *A.I.A.A Journal*, 28(8):1415 – 1425, 1990.

[14] K. Mer. *Modèle de viscosités du quatrième ordre pour l'advection-diffusion en maillage non-structuré*. PhD thesis, Université de Nice-Sophia-Antipolis, 1996.

[15] E. Oñate and S.R. Idelsohn. A comparison between finite element and finite volume methods in CFD. In *Computational Fluid Dynamics'92*, 1992.

[16] H. Paillère and H. Deconinck. Compact multidimensional upwind convection schemes on unstructured meshes. Proceedings of the CERCA, Conference on Numerical Methods for the Euler and Navier-Stokes Equations, 1995.

[17] H. Paillère, H. Deconinck, and P. L. Roe. Conservative upwind residual-distribution schemes based on the steady characteristics of the Euler equations. *AIAA paper 1700*, 1995.

[18] V. Selmin and L. Formaggia. Unified construction of finite element and finite volume discretizations for compressible flows. *Int. J. for Num. Meth. in Eng.*, 39:1 – 32, 1996.

[19] D. Sidilkover. A genuinely multidimensional upwind scheme and efficient multigrid solver for the compressible Euler equations. Technical Report 94-84, ICASE, 1994.

[20] D. Sidilkover. Multidimensional upwind and multigrid. *AIAA paper 1759*, 1995.

[21] R. Struijs, H. Deconinck, and P.L. Roe. Fluctuation splitting schemes for 2D Euler equations. *Computational Fluid Dynamics*, 1991. In von Karmann Institute Lecture Series 1991-01.

[22] B. van Leer. Towards the ultimate conservative difference scheme i. the quest of monotonicity. *Lectures notes in Physics*, 18:163, 1972.

Appendix I. Relation to existing finite-volume schemes

The purpose of this appendix is to verify that choosing a particular barycenter with weights (α_s, α_m, α_l) for the Barycentered Diamond scheme is equivalent to choosing a Finite-Volume scheme relying on a barycenter C of the vertices with weights (λ_s, λ_m, λ_l). We use the notation of Figure 17.

We write $\left(\nu_{mn}^T\right)_l$ as the normal of a cell built by joining the middle of each edge of the triangle (I_{sm}, I_{ml}, I_{ls}) to a point C in the triangle,

$$\left(\nu_{mn}^T\right)_l \quad = \quad \begin{cases} (C\vec{I}_{sm})^\perp & \text{if} \quad \vec{mn} = s\vec{m}, \\ (C\vec{I}_{sl})^\perp & \text{if} \quad \vec{mn} = \vec{ls}, \\ (C\vec{I}_{ml})^\perp & \text{if} \quad \vec{mn} = l\vec{m}. \end{cases} \tag{79}$$

In order to determine the barycenter corresponding to this scheme, we will write $\left(\nu_{mn}^T\right)_l$ in terms of $s\vec{m}$, $\vec{ml}$ and $\vec{ls}$.

Properties of the barycenter coordinates:

Property 1:

$$\vec{CP} = \lambda_s^c \, \vec{sP} + \lambda_m^c \, \vec{mP} + \lambda_l^c \, \vec{lP}, \qquad \forall C \text{ of T}, \forall P, \tag{80}$$

Property 2:

$$\lambda_s^c + \lambda_m^c + \lambda_l^c = 1. \tag{81}$$

Writing (80) for the particular cases where P is equal to I_{sm}, I_{ml} and I_{sl}, we obtain:

$$\begin{cases} \vec{CI}_{sm} &= \lambda_s^c \, \vec{sI}_{sm} &+ \lambda_m^c \, \vec{mI}_{sm} &+ \lambda_l^c \, \vec{kI}_{sm}, \\ \vec{CI}_{ml} &= \lambda_s^c \, \vec{sI}_{ml} &+ \lambda_m^c \, \vec{mI}_{ml} &+ \lambda_l^c \, \vec{lI}_{ml}, \\ \vec{CI}_{sl} &= \lambda_s^c \, \vec{sI}_{ls} &+ \lambda_m^c \, \vec{mI}_{ls} &+ \lambda_l^c \, \vec{lI}_{ls}. \end{cases} \tag{82}$$

Since by definition I_{sm}, I_{ml}, I_{ls} are the middle of respectively, $\vec{sm}$, $\vec{ml}$ and $\vec{ls}$, for any point P we can write

$$\begin{cases} P\vec{I}_{sm} = \frac{1}{2}(\vec{Ps} + \vec{Pm}), \\ P\vec{I}_{ml} = \frac{1}{2}(\vec{Pm} + \vec{Pl}), \\ P\vec{I}_{ls} = \frac{1}{2}(\vec{Pl} + \vec{Ps}). \end{cases} \tag{83}$$

In particular, Equations (83) are verified in the case where the point P is equal to s, m or l which enables us to express vectors involving the middle points in Equations (82) in terms of the vertices of the triangle. Equations (82) become

$$\begin{cases} (C\vec{I}_{sm})^{\perp} &= \frac{1}{2}\left((1-2\,\lambda_s^c)\,(\vec{ls})^{\perp} + (1-2\,\lambda_m^c)\,(\vec{lm})^{\perp}\right), \\ (C\vec{I}_{ml})^{\perp} &= \frac{1}{2}\left((1-2\,\lambda_m^c)\,(\vec{sm})^{\perp} + (1-2\,\lambda_l^c)\,(\vec{sl})^{\perp}\right), \\ (C\vec{I}_{ls})^{\perp} &= \frac{1}{2}\left((1-2\,\lambda_l^c)\,(\vec{ml})^{\perp} + (1-2\,\lambda_s^c)\,(\vec{ms})^{\perp}\right). \end{cases} \tag{84}$$

Identifying Equations (84) with Equations (49) (in which the numbers i, j and k have been replaced by s, m and l respectively), we obtain

$$\begin{cases} \alpha_s = 1 - 2\,\lambda_s^c, \\ \alpha_m = 1 - 2\,\lambda_m^c, \\ \alpha_l = 1 - 2\,\lambda_l^c. \end{cases} \tag{85}$$

Equations (85) give the relation which, with any point C used to build a finite-volume cell, associates a barycenter with weights (α_s, α_m, α_l). Particular cases are presented in Table 1.

Unité de recherche INRIA Sophia Antipolis
2004, route des Lucioles - B.P. 93 - 06902 Sophia Antipolis Cedex (France)

Unité de recherche INRIA Lorraine : Technopôle de Nancy-Brabois - Campus scientifi que
615, rue du Jardin Botanique - B.P. 101 - 54602 Villers lès Nancy Cedex (France)
Unité de recherche INRIA Rennes : IRISA, Campus universitaire de Beaulieu - 35042 Rennes Cedex (France)
Unité de recherche INRIA Rhône-Alpes : 655, avenue de l'Europe - 38330 Montbonnot St Martin (France)
Unité de recherche INRIA Rocquencourt : Domaine de Voluceau - Rocquencourt - B.P. 105 - 78153 Le Chesnay Cedex (France)

Éditeur
INRIA - Domaine de Voluceau - Rocquencourt, B.P. 105 - 78153 Le Chesnay Cedex (France)
http://www.inria.fr
ISSN 0249-6399